

## Electronic supplementary information for the paper

### Synthesis and structure of 7-thiabicyclo[2.2.1]heptenes: functional complementarity of the sulfur atom and the ethenyl fragment

by Alexandra G. Kutasevich, Eugeniya V. Nikitina, Yana S. Novoselskaya, Mikhail S. Grigoriev, Vadim V. Brazhkin, Reza Kia, Fedor I. Zubkov, Rosa M. Gomila and Antonio Frontera

<sup>a</sup> Department of Organic Chemistry, RUDN University, 117198 Moscow, Russian Federation.  
Fedor I. Zubkov [zubkov\\_fi@pfur.ru](mailto:zubkov_fi@pfur.ru) and [fzubkov1973@gmail.com](mailto:fzubkov1973@gmail.com)

Alexandra G. Kutasevich [alexandra.podrezova@mail.ru](mailto:alexandra.podrezova@mail.ru)

Eugeniya V. Nikitina [nikitina-ev1@rudn.ru](mailto:nikitina-ev1@rudn.ru)

Yana S. Novoselskaya [1032216580@pfur.ru](mailto:1032216580@pfur.ru)

<sup>b</sup> Frumkin Institute of Physical Chemistry and Electrochemistry, Russian Academy of Sciences, 119071 Moscow, Russia.

Mikhail S. Grigoriev [mickgrig@mail.ru](mailto:mickgrig@mail.ru)

<sup>c</sup> Institute for High Pressure Physics, Russian Academy of Sciences, 14, Kaluzhskoe shosse, 108840, Troitsk, Moscow, Russia.

Vadim V. Brazhkin [brazhkin@hppi.troitsk.ru](mailto:brazhkin@hppi.troitsk.ru)

<sup>d</sup> Chemistry Department, Sharif University of Technology, P.O. Box 11155-3516, Tehran, Iran.

Reza Kia [rkia@sharif.edu](mailto:rkia@sharif.edu)

<sup>e</sup> Department of Chemistry, Universitat de les Illes Balears, Crta. de Valldemossa km 7.5, 07122 Palma de Mallorca (Balears), SPAIN

Rosa M. Gomila [rosagomilaribas@gmail.com](mailto:rosagomilaribas@gmail.com)

Antonio Frontera [toni.frontera@uib.es](mailto:toni.frontera@uib.es)

#### TABLE OF CONTENTS

<b>1. Experimental part</b> .....	2
<b>2. Copies of NMR and IR spectra of the <i>exo</i>-1 and <i>endo</i>-1 diastereoisomers</b> .....	5
<b>3. Piston-cylinder high-pressure apparatus</b> .....	9
<b>4. XRD description</b> .....	15
<b>5. Computational Chemistry Details</b> .....	25
<b>5.1. Intra- and intermolecular interactions</b> .....	25
<b>5.2. Interaction energy and energy decomposition analysis (EDA)</b> .....	30
<b>6. X-ray phase analysis of polycrystalline samples <i>exo</i>-1B, <i>endo</i>-1 and mixed crystals 3</b> .....	32
<b>References for ESI</b> .....	34

## 1. Experimental part

### General methods

Starting reagents were purchased from commercial sources and were used without any additional purification. The routine  $^1\text{H}$  and  $^{13}\text{C}$  NMR spectra were acquired on a Jeol JNM-ECA 600 spectrometer (with operating frequencies of 600 and 150 MHz for  $^1\text{H}$  and  $^{13}\text{C}$ , respectively) at r.t and referenced to the residual signals of  $\text{CDCl}_3$ . Chemical shifts are reported in parts per million ( $\delta/\text{ppm}$ ) referenced to an internal solvent signal. Coupling constants are reported in Hertz ( $J/\text{Hz}$ ). The peak patterns are indicated as follows: s, singlet; d, doublet; t, triplet; q, quadruplet; m, multiplet; dd, doublet of doublets; ddd, doublet of doublet of doublets; tt, triplet of triplets, and br s, broad singlet. Infrared spectra were measured on an Infracum FT-801 FTIR instrument. The wavelengths are reported in reciprocal centimeters ( $\nu_{\text{max}}/\text{cm}^{-1}$ ). HRMS spectra were recorded on a tandem quadrupole time-of-flight (QTOF) accurate mass detector (Agilent 6545 Q-TOF LC/MS; Agilent Technologies, USA). Melting points were determined on a SMP 10 apparatus and not corrected. Solvents were distilled and dried according to standard procedures, silica gel 5–40  $\mu$  was used for filtration.

(3a*RS*,4*RSR*,7a*SR*)-2-Phenyl-3a,4,7,7a-tetrahydro-1*H*-4,7-epithioisindole-1,3(2*H*)-dione (**1-*exo***) and (3a*RS*,4*SR*,7*RS*,7a*SR*)-2-phenyl-3a,4,7,7a-tetrahydro-1*H*-4,7-epithioisindole-1,3(2*H*)-dione (**1-*endo***).

*General procedure for the “combined method” (pressure + LA at r.t)*

A solution of  $\text{AlCl}_3$  (6 mL, c ~ 0.55 mmol/mL) in dry dichloromethane (DCM) was added to a solution of N-phenylmaleimide (2.6 g, 15 mmol) and thiophene (2.4 mL, 30 mmol) in dry DCM (13 mL). Resulting mixture was transferred in a PTFE vial (~ 21  $\text{cm}^3$ ) and then held at 12 kbar and r.t. for two days in a piston-cylinder type steel pressure chamber (see the ESI). The obtained DCM solution was quenched with few drops of water and filtered through thin silica gel layer using DCM as an eluent. The resulting filtrate was concentrated *in vacuo* and treated with hexane (20 mL). After filtration of the precipitate, a slight yellow solid (~ 3.5 g) was obtained. The ratio of the **1-*exo***/**1-*endo*** isomers was 51/45 according to  $^1\text{H}$  NMR analysis of the crude reaction mixture. The resulting solid was purified by column chromatography on silica gel using a mixture of PhH/EtOAc (80:20) as an eluent. The purified fractions were concentrated *in vacuo* and dried under reduced

pressure in a vacuum desiccator to constant weight, yielding the target products as white crystals. Fractions, containing mixtures of the isomers, were not analyzed.

**exo-1.** White solid, 1.54 g, yield 42%.  $R_f$  0.52, “Sorbfil” plates for thin-layer chromatography (PhH/EtOAc, 80:20). M.p: 185–186 °C (from EtOAc). A single-crystal of **exo-1(B)** was obtained by a slow recrystallization from EtOH, **exo-1(A)** – from EtOAc.  $^1\text{H}$  NMR (700 MHz,  $\text{CDCl}_3$ , 298 K)  $\delta$  7.43 – 7.35 (m, 2H), 7.35 – 7.25 (m, 1H), 7.18 (d,  $J$  = 7.6 Hz, 2H), 6.55 (s, 2H), 4.49 (s, 2H), 3.23 (s, 2H) ppm.  $^{13}\text{C}$  NMR (175 MHz,  $\text{CDCl}_3$ , 298 K)  $\delta$  175.33, 140.09, 131.99, 129.33, 129.02, 126.69, 54.03, 50.26 ppm. IR  $\nu_{\text{max}}/\text{cm}^{-1}$  (KBr): 3647, 3512, 3450, 3066, 1704, 1497, 1384, 1197, 1166. HRMS (ESI-TOF): calculated for  $\text{C}_{14}\text{H}_{11}\text{NO}_2\text{S}$  [ $\text{M} + \text{Na}$ ]: 280.0403, found: 280.0398 [ $\text{M} + \text{Na}$ ] $^+$ .

**endo-1.** White solid, 1.29 g, yield 31%.  $R_f$  0.72, “Sorbfil” plates for thin-layer chromatography, PhH/EtOAc, 80:20. M.p: 172–173 °C (from EtOAc).

$^1\text{H}$  NMR (700 MHz,  $\text{CDCl}_3$ , 298 K)  $\delta$  7.45 – 7.41 (m, 2H), 7.40 – 7.35 (m, 1H), 7.12 (d,  $J$  = 7.5 Hz, 2H), 6.58 (t,  $J$  = 2.1 Hz, 2H), 4.59 (s, 2H), 4.03 (s, 2H) ppm.  $^{13}\text{C}$  NMR (175 MHz,  $\text{CDCl}_3$ , 298 K)  $\delta$  174.10, 136.89, 131.49, 129.28, 128.98, 126.51, 53.08, 51.09 ppm. IR  $\nu_{\text{max}}/\text{cm}^{-1}$  (KBr): 3613, 3545, 3078, 3016, 1705, 1499, 1387, 1204, 1191. HRMS (ESI-TOF): calculated for  $\text{C}_{14}\text{H}_{11}\text{NO}_2\text{S}$  [ $\text{M} + \text{Na}$ ]: 280.0403, found: 280.0396 [ $\text{M} + \text{Na}$ ] $^+$ .

*Reproducing of the “pressure method”<sup>6</sup> (for ref. see the main part)*

A mixture of thiophene (21 mL, 0.262 mol) and N-phenylmaleimide (2.1 g, 12 mmol) was placed in a PTFE vial ( $\sim 21 \text{ cm}^3$ ) and the mixture was allowed to react at 8–10 kbar pressure and 95–105 °C for 2 days. After cooling of the reaction mixture and the release of pressure, an excess of thiophene was evaporated and the crude solid mass ( $\sim 2.85 \text{ g}$ ) was purified by column chromatography on silica gel using a mixture of PhH/EtOAc (80:20) as an eluent to give **exo-1** (1.17 g, 38%) and **endo-1** (0.96 g, 31%) as white solids. The ratio of the **exo-1/endo-1** isomers was  $\sim 50/50$  according to  $^1\text{H}$  NMR analysis of the crude reaction mixture. Fractions, containing mixtures of the isomers, were not analyzed.

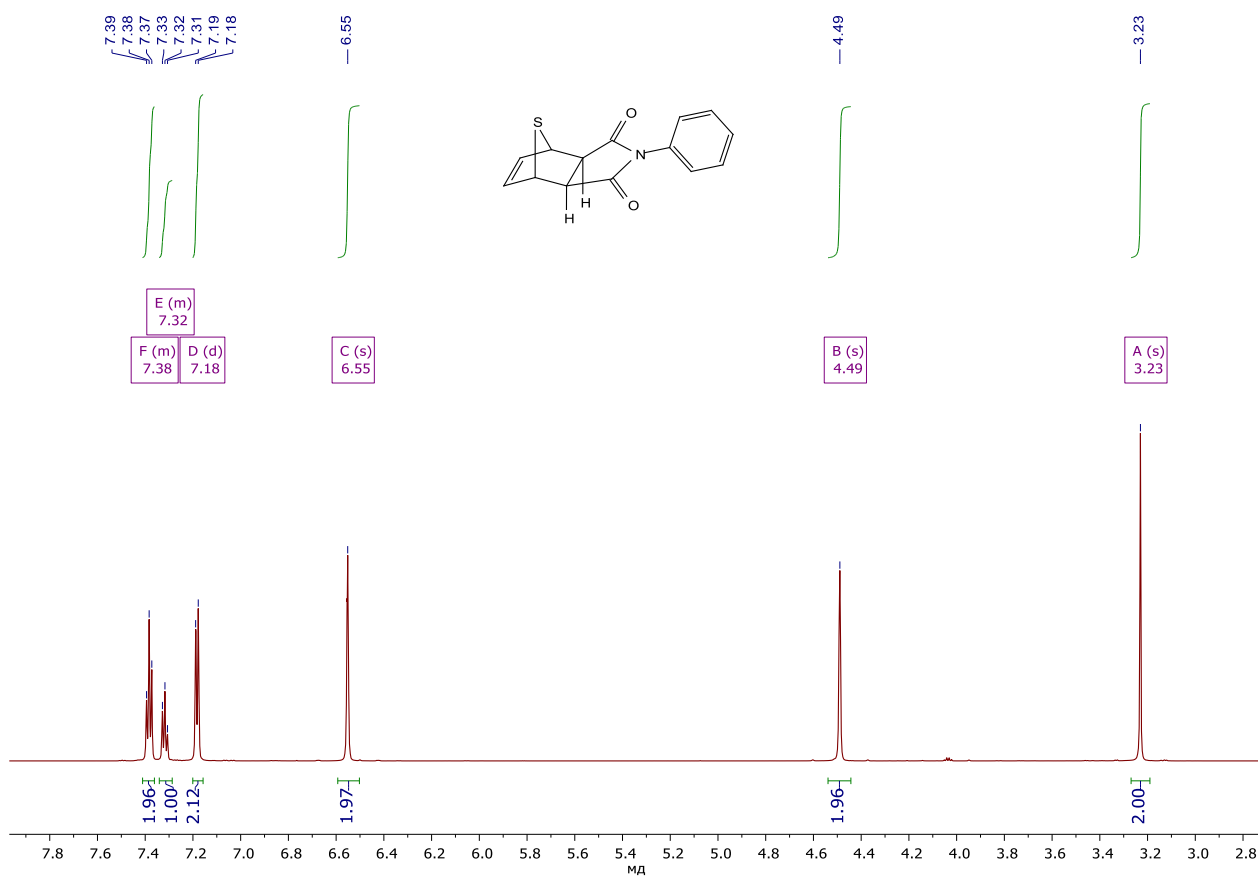
*Reproducing of the “LA method at r.t.”<sup>10</sup> (for ref. see the main part)*

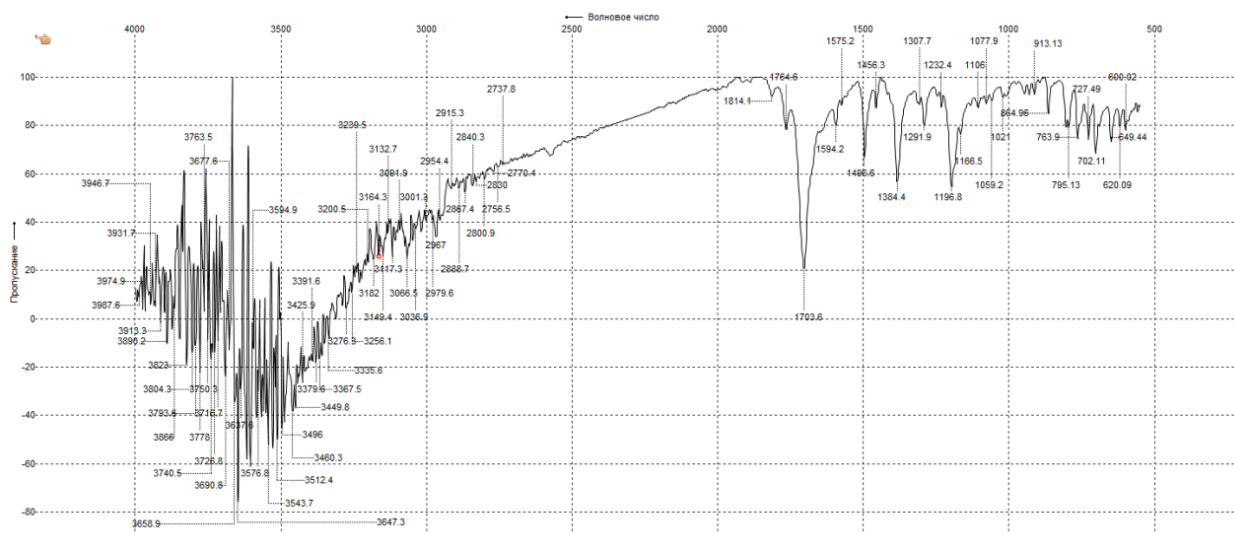
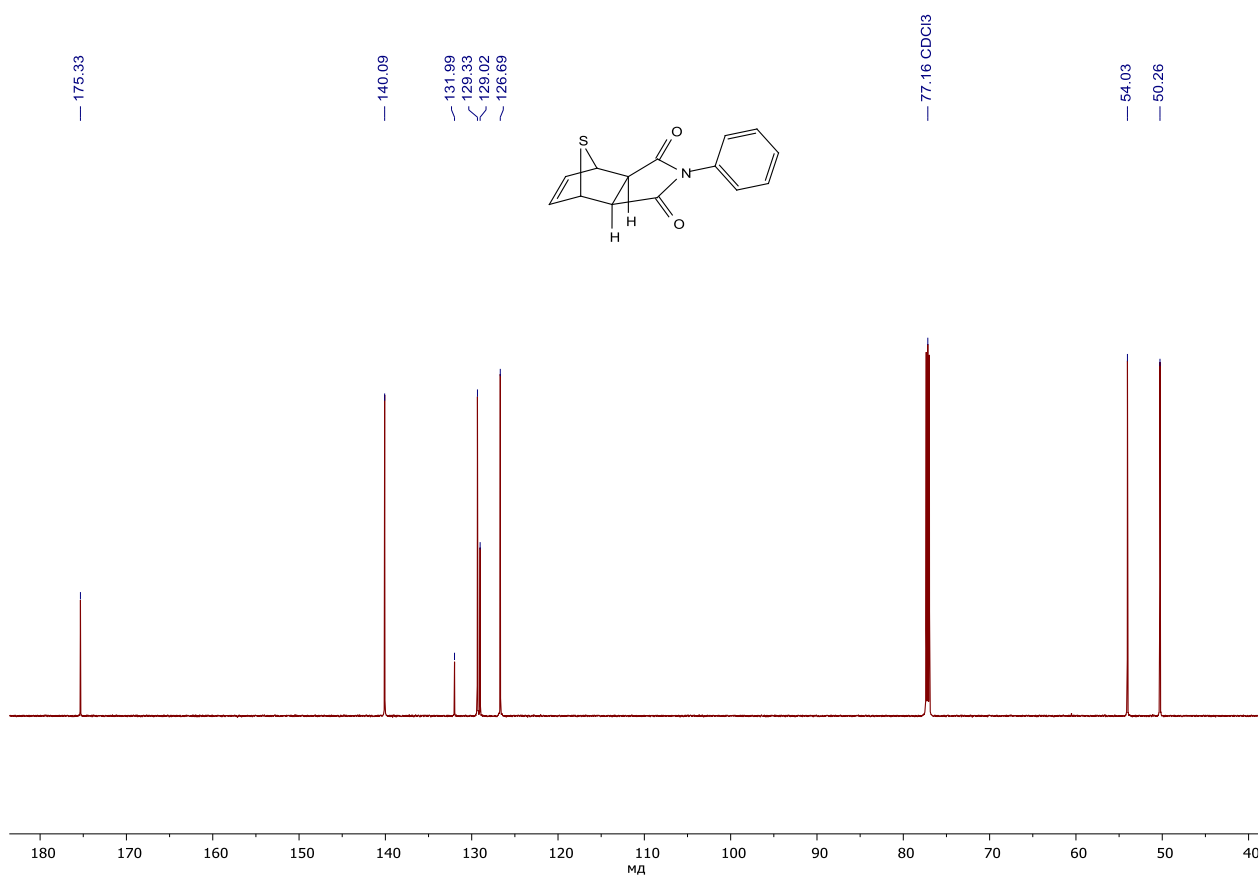
Pulverized anhydrous  $\text{AlCl}_3$  (1.72 g, 13 mmol) was added to a solution of N-phenylmaleimide (2.2 g, 13 mmol) and thiophene (5 mL, 5 equiv) in dry dichloromethane

(60 mL). The mixture was stirred at r.t. for four days in a sealed container. Then, under constant stirring, the reaction mass was quenched with water (~ 1 mL), passed through a thin layer of silica gel and washed with methylene chloride ( $5 \times 100$  mL). The solvent was evaporated under reduced pressure, and the slight yellow residue was purified by double recrystallization from EtOAc, yielding the target ***exo-1*** (1.0 g, 32%) as white crystals.

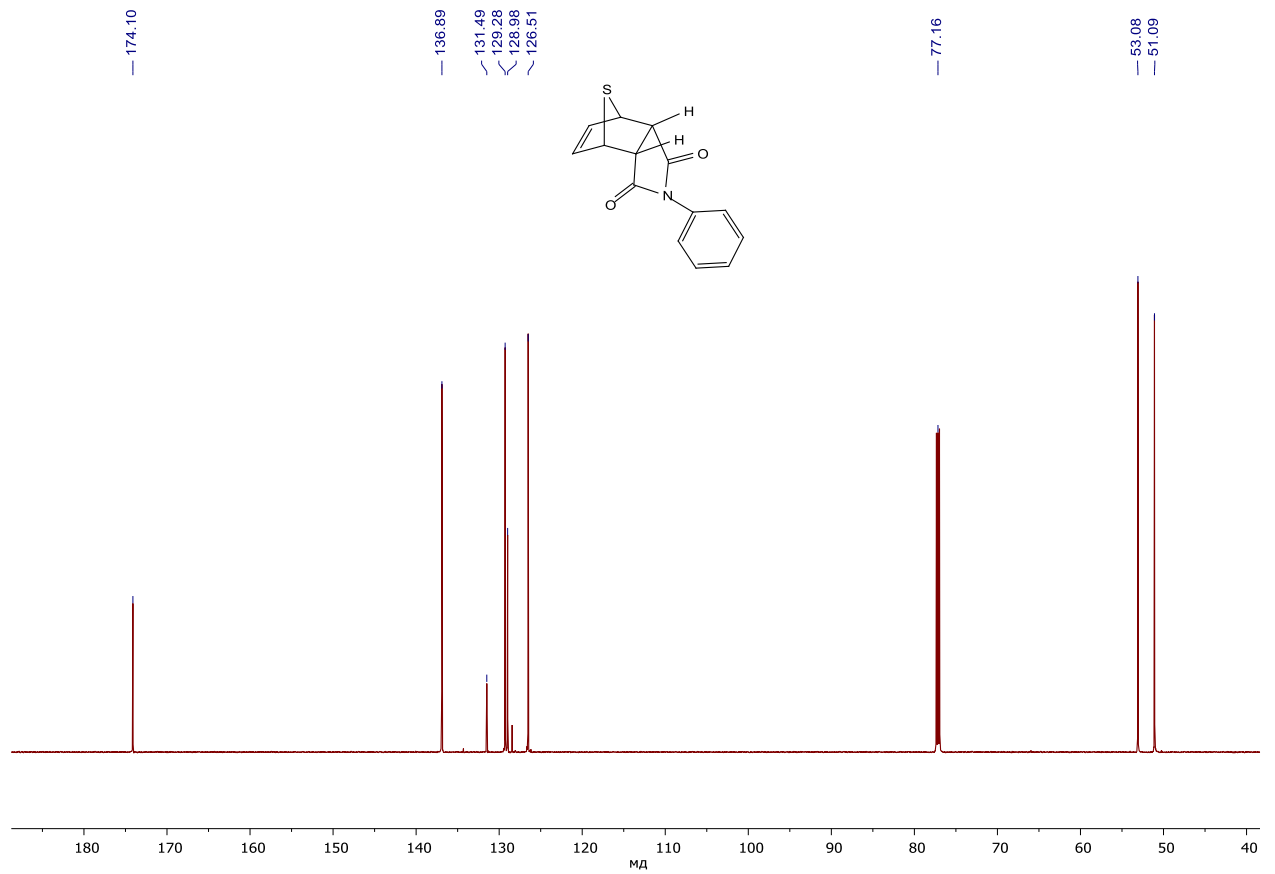
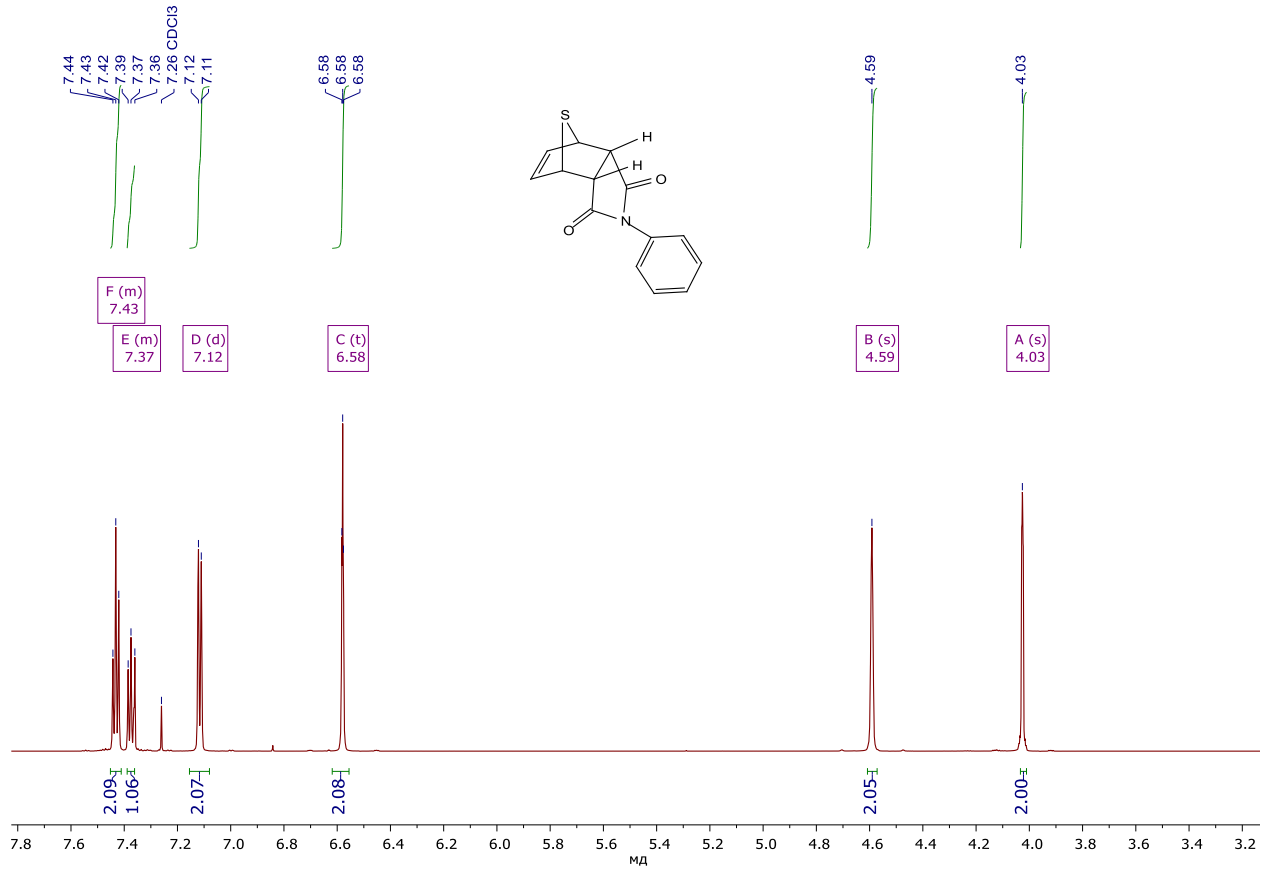
## 2. Copies of NMR and IR spectra of the *exo*-1 and *endo*-1 diastereoisomers

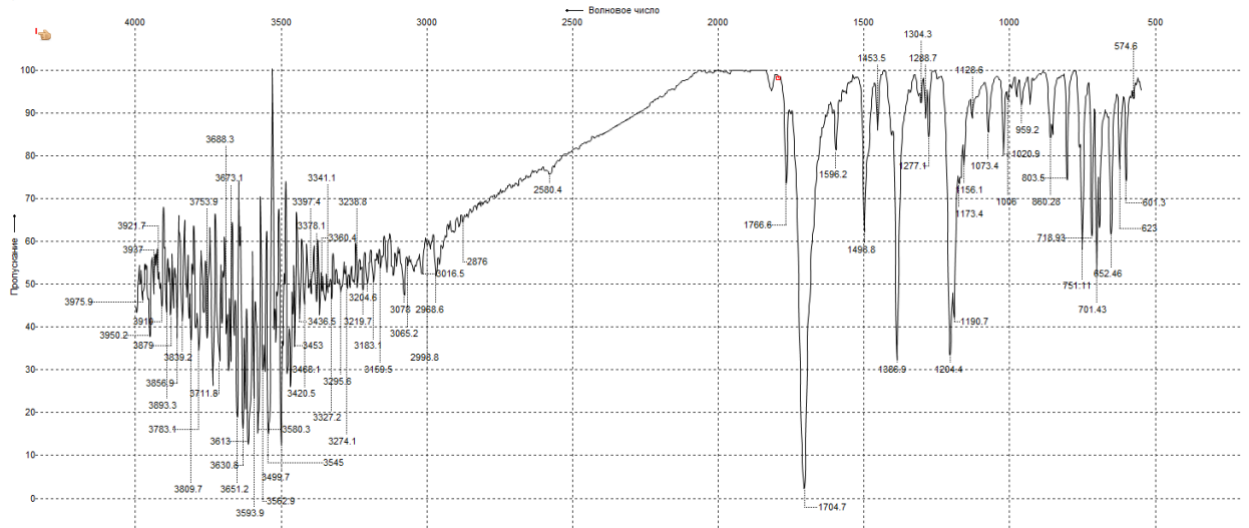
(3*aRS*,4*RSR*,7*aSR*)-2-Phenyl-3*a*,4,7,7*a*-tetrahydro-1*H*-4,7-epithioisindole-1,3(2*H*)-dione (*exo*-1).





(3aRS,4SR,7RS,7aSR)-2-Phenyl-3a,4,7,7a-tetrahydro-1H-4,7-epithioisindole-1,3(2H)-dione  
(endo-1).

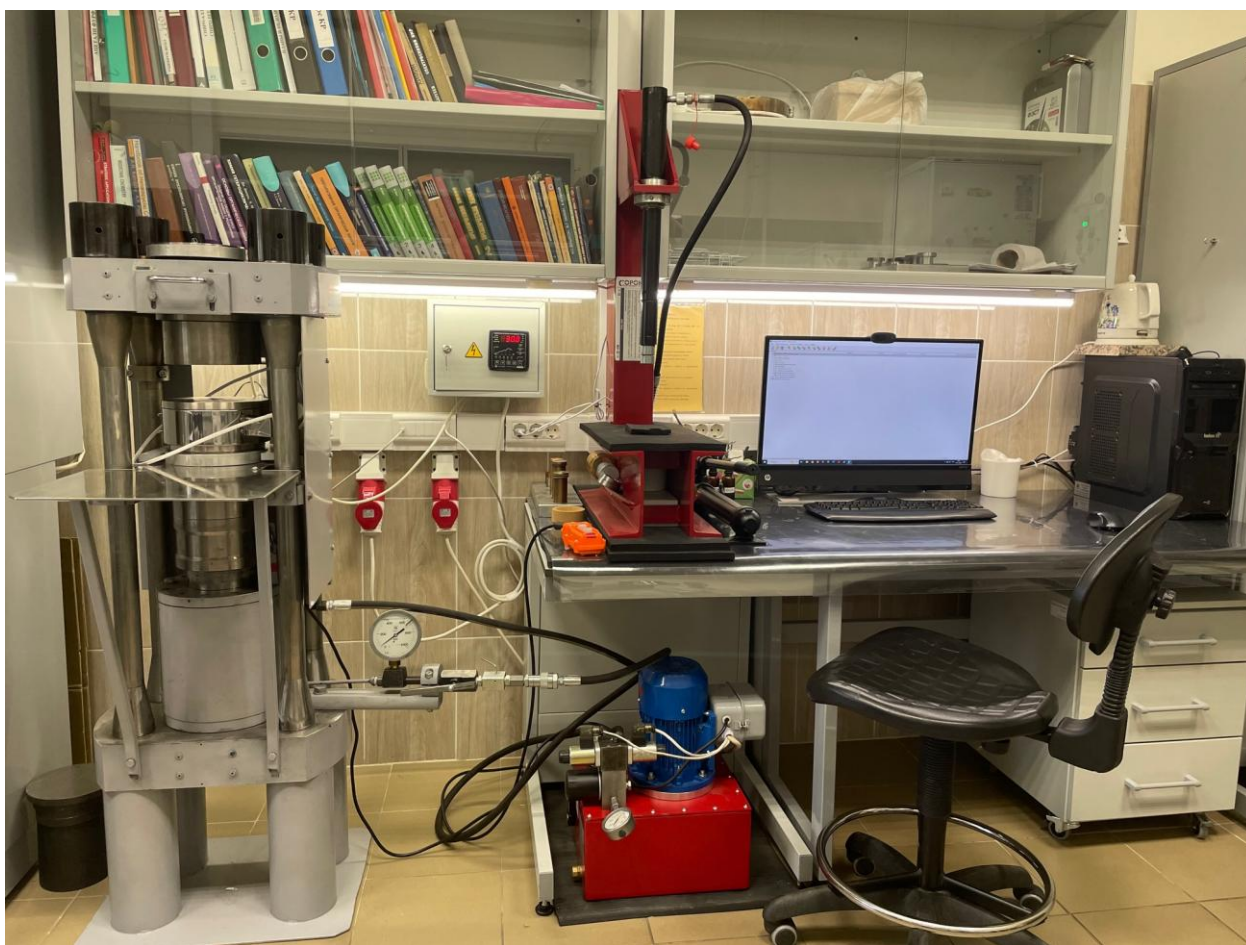




### 3. Piston-cylinder high-pressure apparatus

A piston-cylinder chamber was used as a high-pressure apparatus for studying chemical reactions. The hyperbaric apparatus operator's workplace is shown in Photo S1 (high-pressure apparatus with a piston-cylinder chamber, compressor, unloading press, personal computer with software), individual components and consumables are shown in Photos S2–6.

All reactions were carried out in a piston-cylinder ultrahigh pressure apparatus at a pressure of about 15 kbar. The initial working volume was 21 mL. The high-pressure vessel consisted of two outer steel rings, into which an inner cylindrical PTFE vessel with a cap was placed. The inner vessel was pressed into the support rings by a hydraulic press piston in a well-controlled manner depending on the internal pressure. The cylindrical high-pressure volume was closed at the bottom with a steel plug. Sealing of the mobile piston and the stopper were attained by using brass O-rings. For the reactions performed at the elevated temperatures external heating jacket was employed.



**Photograph S1.** Workplace of hyperbaric apparatus operator's

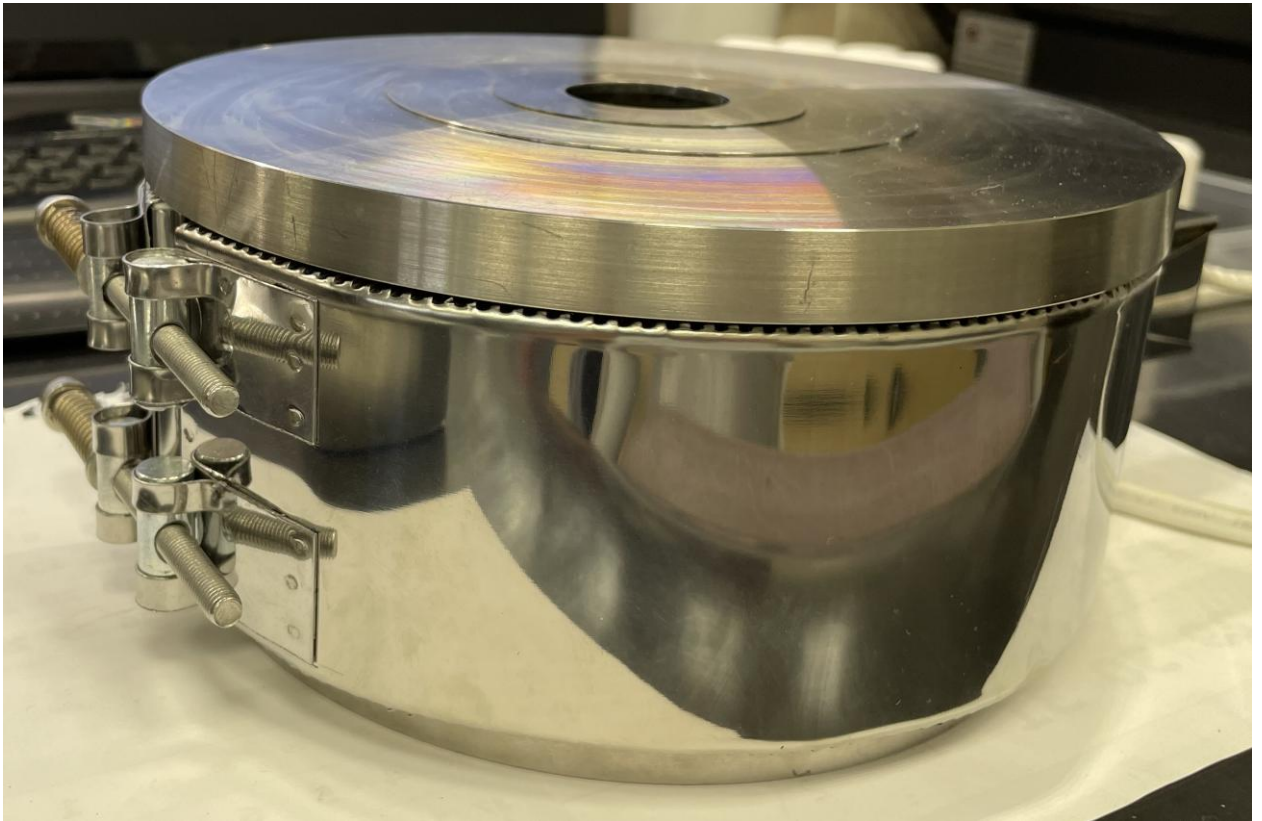




**Photograph S2.** Hyperbaric apparatus with a closed steel protective cell door of a piston-cylinder chamber



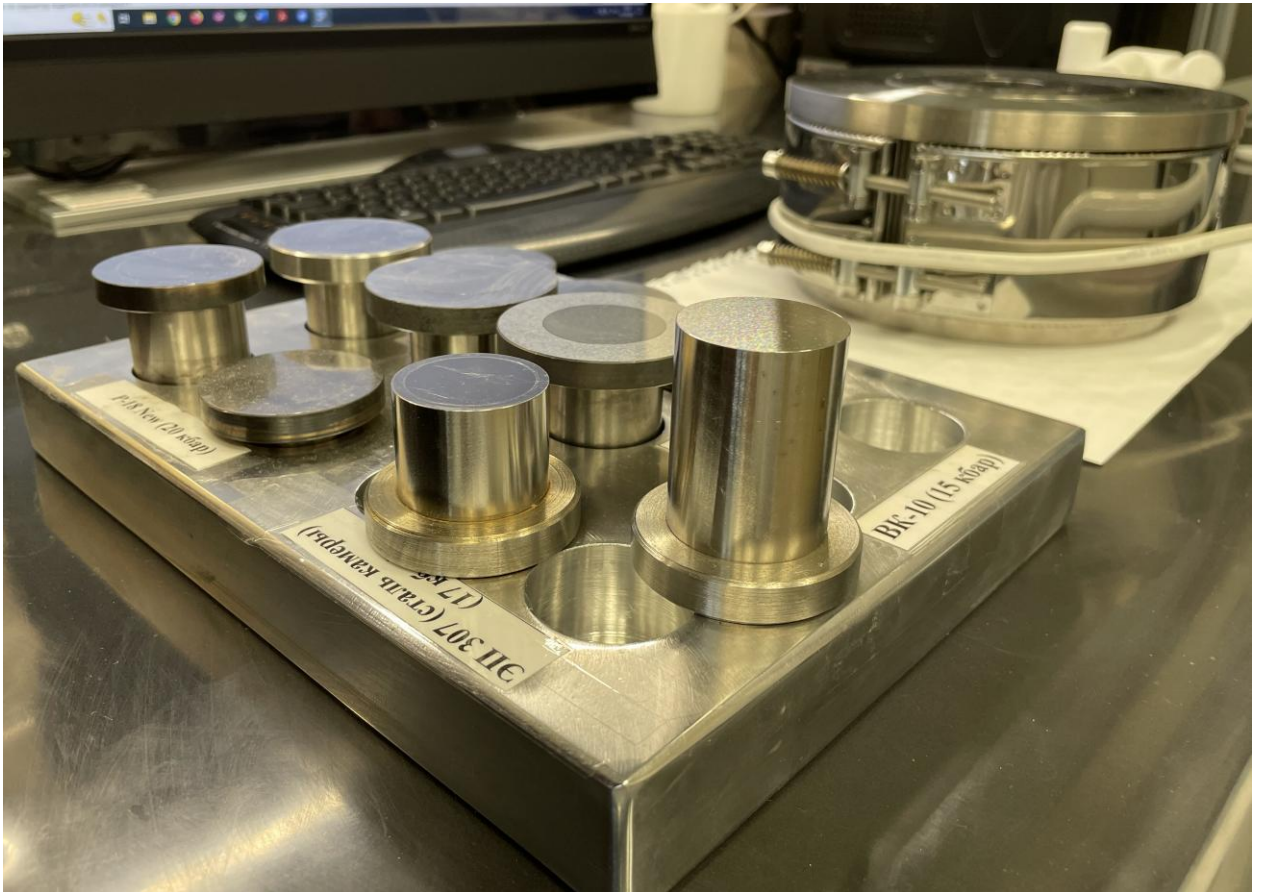
**Photograph S3.** Cell with a piston-cylinder chamber and a heating element



**Photograph S4.** Piston-cylinder chamber equipped with a heating element



**Photograph S5.** Teflon ampoules with an internal volume of 22 cm<sup>3</sup>.



**Photograph S6.** Set of pistons for the hyperbaric apparatus

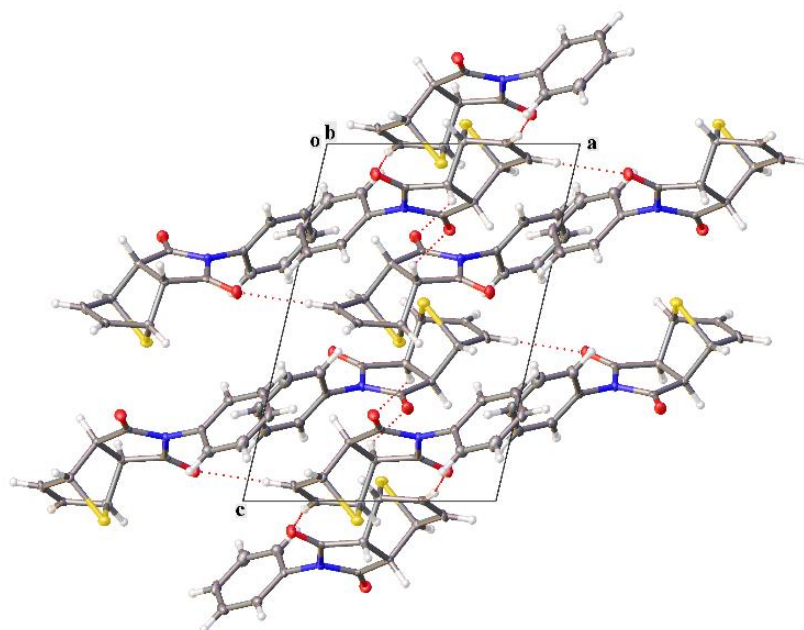
#### 4. XRD description

A detailed description of the molecular packing of the synthesized compounds is given in the main part of the article. Some other parameters of the molecular packing of the polymorphs and mixed crystals *exo-1(A)*, *exo-1(B)*, **3** and **4** are given below.

The crystal packing in all structures *exo-1*, **3** and **4** is different (see Figs. S1–S4). A number of H-bonds of C–H $\cdots$ O type is present. In **4**, the molecules are combined into pairs by  $\pi$ - $\pi$  interaction between parallel phenyl rings (centroid-centroid distance 3.942 Å, shift distance 1.846 Å).

Bond lengths, bond angles, hydrogen bonds, and torsion angles for the molecules *exo-1(A)*, *exo-1(B)*, **3** and **4** are given in Tables S1–S16.

---



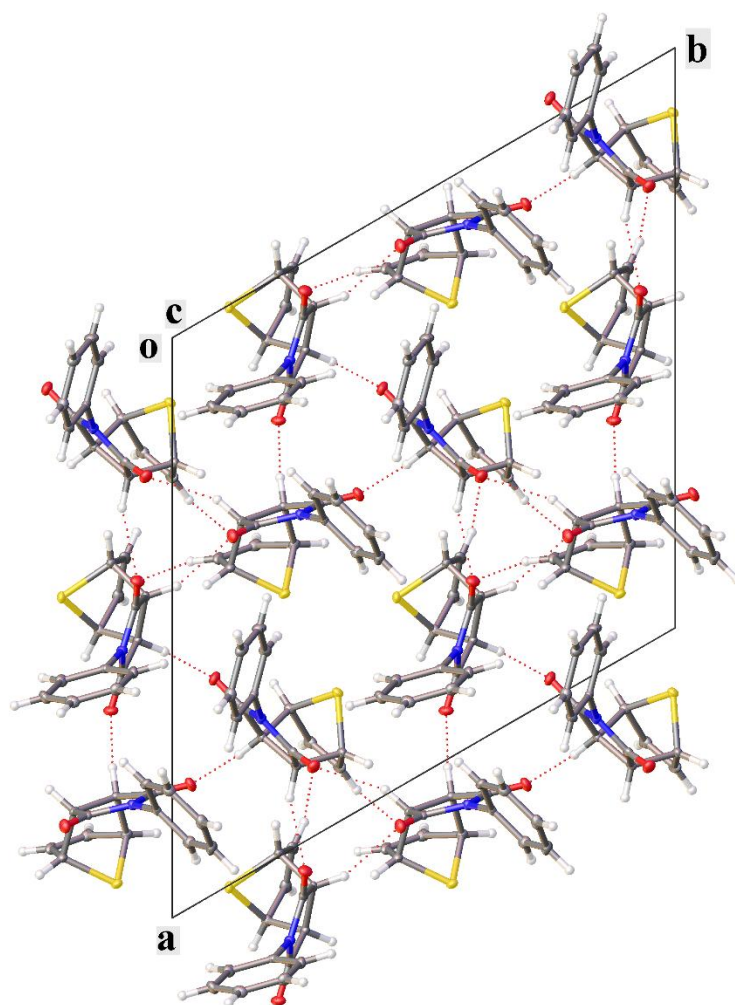


**Figure S1.** Molecular packing of polymorphs *exo-1(A)* (top) and *exo-1(B)* (bottom)

---

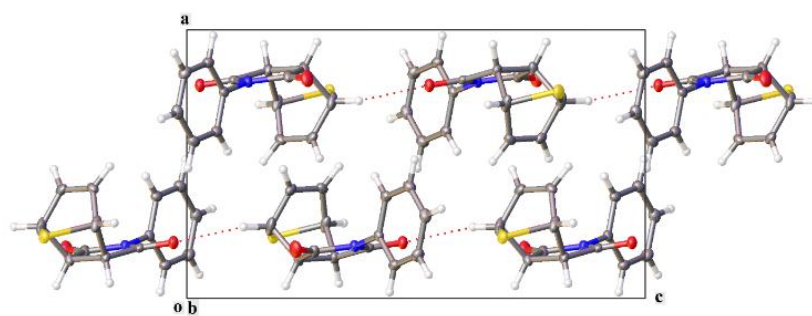


**Figure S2.** Molecular packing of the mixed crystals **3**

---

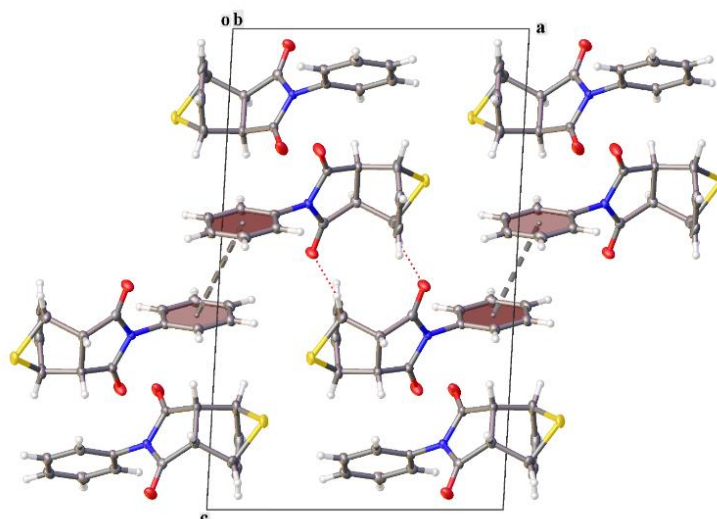


Figure S3. Molecular packing of the mixed crystals 4

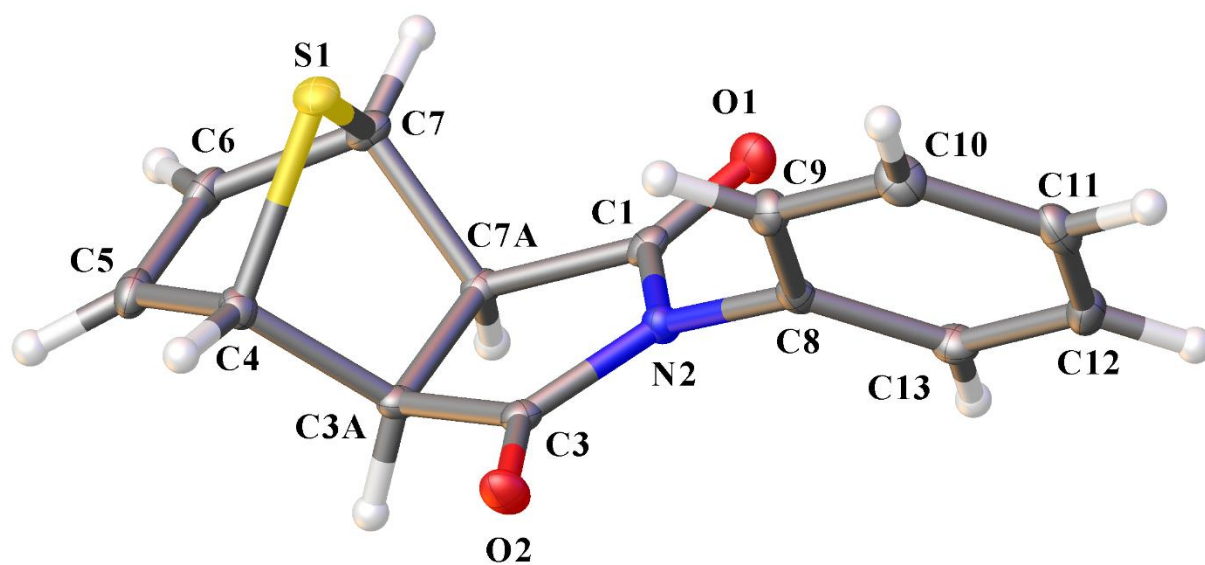


Figure S4. Molecular structure of *exo*-1(B)

Table S1. Bond Lengths for *exo*-1(A)

Atom	Atom	Length/Å	Atom	Atom	Length/Å
S1	C4	1.839(2)	C4	C5	1.523(3)
S1	C7	1.846(2)	C5	C6	1.299(3)
O1	C1	1.207(3)	C6	C7	1.518(3)
O2	C3	1.212(2)	C7	C7A	1.558(3)
N2	C1	1.403(3)	C8	C9	1.381(3)
N2	C3	1.402(3)	C8	C13	1.385(3)
N2	C8	1.434(3)	C9	C10	1.389(3)
C1	C7A	1.508(3)	C10	C11	1.388(3)
C3	C3A	1.505(3)	C11	C12	1.383(3)

Atom	Atom	Length/Å	Atom	Atom	Length/Å
C3A	C4	1.561(3)	C12	C13	1.385(3)
C3A	C7A	1.539(3)			

Table S2. Bond Angles for *exo*-1(A)

Atom	Atom	Atom	Angle/°	Atom	Atom	Atom	Angle/°
C4	S1	C7	79.64(10)	C6	C5	C4	110.2(2)
C1	N2	C8	122.93(19)	C5	C6	C7	110.6(2)
C3	N2	C1	112.62(18)	C6	C7	S1	101.86(14)
C3	N2	C8	123.98(19)	C6	C7	C7A	104.86(17)
O1	C1	N2	124.0(2)	C7A	C7	S1	101.83(14)
O1	C1	C7A	127.7(2)	C1	C7A	C3A	105.17(17)
N2	C1	C7A	108.25(19)	C1	C7A	C7	112.62(17)
O2	C3	N2	124.1(2)	C3A	C7A	C7	105.60(15)
O2	C3	C3A	127.7(2)	C9	C8	N2	119.45(19)
N2	C3	C3A	108.20(19)	C9	C8	C13	120.3(2)
C3	C3A	C4	112.70(16)	C13	C8	N2	120.2(2)
C3	C3A	C7A	105.41(17)	C8	C9	C10	120.1(2)
C7A	C3A	C4	104.91(16)	C11	C10	C9	119.8(2)
C3A	C4	S1	101.52(14)	C12	C11	C10	119.7(2)
C5	C4	S1	102.08(15)	C11	C12	C13	120.6(2)
C5	C4	C3A	105.78(16)	C12	C13	C8	119.5(2)

Table S3. Hydrogen Bonds for *exo*-1(A)

D	H	A	d(D-H)/Å	d(H-A)/Å	d(D-A)/Å	D-H-A/°
C3A	H3B	O1 <sup>1</sup>	1.00	2.41	3.249(3)	141.4
C6	H6A	O2 <sup>2</sup>	0.95	2.48	3.415(3)	168.2

<sup>1</sup>1-X,-1/2+Y,3/2-Z; <sup>2</sup>1+X,+Y,+Z

Table S4. Torsion Angles for *exo*-1(A)

A	B	C	D	Angle/°	A	B	C	D	Angle/°
S1	C4	C5	C6	38.96(19)	C3A	C4	C5	C6	-66.9(2)
S1	C7	C7A	C1	-72.84(18)	C4	S1	C7	C6	50.13(14)
S1	C7	C7A	C3A	41.41(18)	C4	S1	C7	C7A	-58.03(14)
O1	C1	C7A	C3A	-177.27(19)	C4	C3A	C7A	C1	120.84(17)
O1	C1	C7A	C7	-62.8(3)	C4	C3A	C7A	C7	1.5(2)
O2	C3	C3A	C4	59.9(3)	C4	C5	C6	C7	0.2(2)
O2	C3	C3A	C7A	173.79(19)	C5	C6	C7	S1	-39.0(2)
N2	C1	C7A	C3A	2.0(2)	C5	C6	C7	C7A	66.8(2)
N2	C1	C7A	C7	116.48(18)	C6	C7	C7A	C1	-178.67(17)
N2	C3	C3A	C4	-118.62(18)	C6	C7	C7A	C3A	-64.4(2)
N2	C3	C3A	C7A	-4.8(2)	C7	S1	C4	C3A	59.00(14)
N2	C8	C9	C10	-177.7(2)	C7	S1	C4	C5	-50.12(13)
N2	C8	C13	C12	178.0(2)	C7A	C3A	C4	S1	-44.11(18)
C1	N2	C3	O2	-172.20(18)	C7A	C3A	C4	C5	62.1(2)
C1	N2	C3	C3A	6.4(2)	C8	N2	C1	O1	1.5(3)
C1	N2	C8	C9	63.3(3)	C8	N2	C1	C7A	-177.76(16)
C1	N2	C8	C13	-114.8(2)	C8	N2	C3	O2	0.2(3)
C3	N2	C1	O1	173.97(18)	C8	N2	C3	C3A	178.78(17)

A	B	C	D	Angle/°	A	B	C	D	Angle/°
C3	N2	C1	C7A	-5.3(2)	C8	C9	C10	C11	-0.5(3)
C3	N2	C8	C9	-108.2(2)	C9	C8	C13	C12	-0.1(3)
C3	N2	C8	C13	73.7(2)	C9	C10	C11	C12	0.1(4)
C3	C3A	C4	S1	70.1(2)	C10	C11	C12	C13	0.2(3)
C3	C3A	C4	C5	176.30(18)	C11	C12	C13	C8	-0.2(3)
C3	C3A	C7A	C1	1.7(2)	C13	C8	C9	C10	0.4(3)
C3	C3A	C7A	C7	-117.65(17)					

Table S5. Bond Lengths for the mixed crystals 3

Atom	Atom	Length/Å	Atom	Atom	Length/Å
S1	C4	1.883(2)	C4	C5	1.427(4)
S1	C7	1.897(2)	C5	C6	1.349(6)
S1A	C4A	2.034(3)	C6	C7	1.426(4)
S1A	C7B	2.027(3)	C7	C7A	1.561(2)
O1	C1	1.209(2)	C4A	C5A	1.312(9)
O2	C3	1.2128(19)	C5A	C6A	1.368(14)
N2	C1	1.397(2)	C6A	C7B	1.300(8)
N2	C3	1.391(2)	C7B	C7A	1.561(2)
N2	C8	1.441(2)	C8	C9	1.389(2)
C1	C7A	1.512(3)	C8	C13	1.388(2)
C3	C3A	1.517(2)	C9	C10	1.388(2)
C3A	C4	1.559(2)	C10	C11	1.387(2)
C3A	C4A	1.559(2)	C11	C12	1.390(2)
C3A	C7A	1.543(2)	C12	C13	1.388(2)

Table S6. Bond Angles for the mixed crystals 3

Atom	Atom	Atom	Angle/°	Atom	Atom	Atom	Angle/°
C4	S1	C7	77.01(9)	C7A	C7	S1	99.32(13)
C7B	S1A	C4A	70.83(10)	C3A	C4A	S1A	98.37(13)
C1	N2	C8	122.93(15)	C5A	C4A	S1A	99.7(3)
C3	N2	C1	113.36(14)	C5A	C4A	C3A	114.1(4)
C3	N2	C8	123.45(14)	C4A	C5A	C6A	114.0(6)
O1	C1	N2	124.57(17)	C7B	C6A	C5A	110.3(6)
O1	C1	C7A	127.39(16)	C6A	C7B	S1A	101.2(3)
N2	C1	C7A	108.04(14)	C6A	C7B	C7A	115.8(4)
O2	C3	N2	124.03(15)	C7A	C7B	S1A	98.88(12)
O2	C3	C3A	127.53(16)	C1	C7A	C3A	105.42(14)
N2	C3	C3A	108.45(14)	C1	C7A	C7	113.06(16)
C3	C3A	C4	113.33(14)	C1	C7A	C7B	113.06(16)
C3	C3A	C4A	113.33(14)	C3A	C7A	C7	104.97(13)
C3	C3A	C7A	104.67(14)	C3A	C7A	C7B	104.97(13)
C7A	C3A	C4	105.12(13)	C9	C8	N2	119.14(15)
C7A	C3A	C4A	105.12(13)	C13	C8	N2	119.60(14)
C3A	C4	S1	99.94(12)	C13	C8	C9	121.25(16)
C5	C4	S1	103.78(16)	C10	C9	C8	119.07(16)
C5	C4	C3A	108.00(19)	C11	C10	C9	120.28(16)
C6	C5	C4	109.9(2)	C10	C11	C12	120.10(17)
C5	C6	C7	111.4(2)	C13	C12	C11	120.17(16)
C6	C7	S1	103.17(18)	C8	C13	C12	119.12(16)
C6	C7	C7A	107.59(18)				

Table S7. Hydrogen Bonds for the mixed crystals 3

D	H	A	d(D-H)/Å	d(H-A)/Å	d(D-A)/Å	D-H-A/°
C3A	H3AA	O1 <sup>1</sup>	1.00	2.44	3.257(2)	138.9
C7	H7	O2 <sup>2</sup>	1.00	2.46	3.389(2)	155.1
C5A	H5A	O1 <sup>3</sup>	0.95	2.19	3.124(7)	166.1

<sup>1</sup>2-X,1/2+Y,3/2-Z; <sup>2</sup>+X,3/2-Y,1/2+Z; <sup>3</sup>+X,1+Y,+Z

Table S8. Torsion Angles for the mixed crystals 3

A	B	C	D	Angle/°	A	B	C	D	Angle/°
S1	C4	C5	C6	-40.4(2)	C3A	C4	C5	C6	65.1(3)
S1	C7	C7A	C1	-160.40(12)	C3A	C4A	C5A	C6A	-60.6(6)
S1	C7	C7A	C3A	-46.01(15)	C4	S1	C7	C6	-48.65(16)
S1A	C4A	C5A	C6A	43.2(6)	C4	S1	C7	C7A	62.01(12)
S1A	C7B	C7A	C1	-65.27(16)	C4	C3A	C7A	C1	120.45(15)
S1A	C7B	C7A	C3A	49.12(16)	C4	C3A	C7A	C7	0.82(19)
O1	C1	C7A	C3A	-178.20(17)	C4	C5	C6	C7	1.1(3)
O1	C1	C7A	C7	-64.1(2)	C5	C6	C7	S1	38.2(2)
O1	C1	C7A	C7B	-64.1(2)	C5	C6	C7	C7A	-66.2(3)
O2	C3	C3A	C4	63.6(2)	C6	C7	C7A	C1	-53.3(2)
O2	C3	C3A	C4A	63.6(2)	C6	C7	C7A	C3A	61.1(2)
O2	C3	C3A	C7A	177.58(15)	C7	S1	C4	C3A	-61.73(12)
N2	C1	C7A	C3A	0.81(18)	C7	S1	C4	C5	49.75(17)
N2	C1	C7A	C7	114.93(15)	C4A	C3A	C7A	C1	120.45(15)
N2	C1	C7A	C7B	114.93(15)	C4A	C3A	C7A	C7B	0.82(19)
N2	C3	C3A	C4	-116.13(15)	C4A	C5A	C6A	C7B	1.6(8)
N2	C3	C3A	C4A	-116.13(15)	C5A	C6A	C7B	S1A	-46.0(6)
N2	C3	C3A	C7A	-2.15(17)	C5A	C6A	C7B	C7A	59.6(6)
N2	C8	C9	C10	179.58(15)	C6A	C7B	C7A	C1	-172.3(4)
N2	C8	C13	C12	-179.94(15)	C6A	C7B	C7A	C3A	-58.0(4)
C1	N2	C3	O2	-176.86(15)	C7A	C3A	C4	S1	45.21(16)
C1	N2	C3	C3A	2.88(18)	C7A	C3A	C4	C5	-62.9(2)
C1	N2	C8	C9	91.7(2)	C7A	C3A	C4A	S1A	-50.14(16)
C1	N2	C8	C13	-88.69(19)	C7A	C3A	C4A	C5A	54.5(4)
C3	N2	C1	O1	176.71(16)	C8	N2	C1	O1	2.4(3)
C3	N2	C1	C7A	-2.33(18)	C8	N2	C1	C7A	-176.60(14)
C3	N2	C8	C9	-82.0(2)	C8	N2	C3	O2	-2.6(2)
C3	N2	C8	C13	97.62(19)	C8	N2	C3	C3A	177.11(13)
C3	C3A	C4	S1	158.92(12)	C8	C9	C10	C11	0.3(3)
C3	C3A	C4	C5	50.8(2)	C9	C8	C13	C12	-0.3(3)
C3	C3A	C4A	S1A	63.57(16)	C9	C10	C11	C12	-0.1(3)
C3	C3A	C4A	C5A	168.2(4)	C10	C11	C12	C13	-0.3(3)
C3	C3A	C7A	C1	0.79(17)	C11	C12	C13	C8	0.5(3)
C3	C3A	C7A	C7	-118.84(15)	C13	C8	C9	C10	-0.1(3)
C3	C3A	C7A	C7B	-118.84(15)					

Table S9. Bond Lengths for the mixed crystals 4

Atom	Atom	Length/Å	Atom	Atom	Length/Å
S1	C4	1.876(2)	C4	C5	1.438(6)
S1	C7	1.874(2)	C4A	C5A	1.372(15)

Atom	Atom	Length/Å	Atom	Atom	Length/Å
S1A	C4A	1.969(4)	C5	C6	1.356(10)
S1A	C7B	1.989(5)	C6	C7	1.439(6)
O1	C1	1.213(2)	C7	C7A	1.559(3)
O2	C3	1.209(2)	C5A	C6A	1.37(3)
N2	C1	1.386(2)	C6A	C7B	1.379(13)
N2	C3	1.397(2)	C7B	C7A	1.559(3)
N2	C8	1.443(2)	C8	C9	1.383(3)
C1	C7A	1.511(3)	C8	C13	1.385(3)
C3	C3A	1.510(3)	C9	C10	1.391(3)
C3A	C4	1.555(3)	C10	C11	1.385(3)
C3A	C4A	1.555(3)	C11	C12	1.393(3)
C3A	C7A	1.535(3)	C12	C13	1.389(3)

Table S10. Bond Angles for the mixed crystals 4

Atom	Atom	Atom	Angle/°	Atom	Atom	Atom	Angle/°
C7	S1	C4	78.03(10)	C5	C6	C7	110.7(4)
C4A	S1A	C7B	73.21(15)	C6	C7	S1	102.9(3)
C1	N2	C3	113.01(16)	C6	C7	C7A	108.3(2)
C1	N2	C8	123.79(15)	C7A	C7	S1	98.92(14)
C3	N2	C8	123.03(16)	C6A	C5A	C4A	109.1(9)
O1	C1	N2	124.54(18)	C5A	C6A	C7B	113.2(10)
O1	C1	C7A	127.14(18)	C6A	C7B	S1A	99.6(5)
N2	C1	C7A	108.32(16)	C6A	C7B	C7A	112.0(6)
O2	C3	N2	123.98(18)	C7A	C7B	S1A	99.56(17)
O2	C3	C3A	127.50(18)	C1	C7A	C3A	105.38(15)
N2	C3	C3A	108.52(16)	C1	C7A	C7	114.48(17)
C3	C3A	C4	114.11(17)	C1	C7A	C7B	114.48(17)
C3	C3A	C4A	114.11(17)	C3A	C7A	C7	105.34(16)
C3	C3A	C7A	104.73(15)	C3A	C7A	C7B	105.34(16)
C7A	C3A	C4	105.38(16)	C9	C8	N2	119.86(18)
C7A	C3A	C4A	105.38(16)	C9	C8	C13	121.37(18)
C3A	C4	S1	99.39(14)	C13	C8	N2	118.73(17)
C5	C4	S1	103.1(3)	C8	C9	C10	119.05(19)
C5	C4	C3A	108.1(2)	C11	C10	C9	120.24(19)
C3A	C4A	S1A	99.66(16)	C10	C11	C12	120.20(19)
C5A	C4A	S1A	103.0(5)	C13	C12	C11	119.8(2)
C5A	C4A	C3A	112.5(5)	C8	C13	C12	119.36(19)
C6	C5	C4	110.1(4)				

Table S11. Hydrogen Bonds for the mixed crystals 4

D	H	A	d(D-H)/Å	d(H-A)/Å	d(D-A)/Å	D-H-A/°
C7	H7	O1 <sup>1</sup>	1.00	2.36	3.337(3)	166.9
C7B	H7B	O1 <sup>1</sup>	1.00	2.48	3.337(3)	143.1

<sup>1</sup>1-X,-Y,1-Z

Table S12. Torsion Angles for the mixed crystals 4

A	B	C	D	Angle/°	A	B	C	D	Angle/°
S1	C4	C5	C6	-39.3(4)	C3A	C4	C5	C6	65.3(4)

A	B	C	D	Angle/°	A	B	C	D	Angle/°
S1	C7	C7A	C1	-161.08(14)	C3A	C4A	C5A	C6A	-64.6(9)
S1	C7	C7A	C3A	-45.80(18)	C4	S1	C7	C6	-49.5(2)
S1A	C4A	C5A	C6A	41.8(9)	C4	S1	C7	C7A	61.71(14)
S1A	C7B	C7A	C1	-68.7(2)	C4	C3A	C7A	C1	122.24(17)
S1A	C7B	C7A	C3A	46.6(2)	C4	C3A	C7A	C7	0.8(2)
O1	C1	C7A	C3A	-179.7(2)	C4	C5	C6	C7	0.1(6)
O1	C1	C7A	C7	-64.5(3)	C4A	C3A	C7A	C1	122.24(17)
O1	C1	C7A	C7B	-64.5(3)	C4A	C3A	C7A	C7B	0.8(2)
O2	C3	C3A	C4	62.8(3)	C4A	C5A	C6A	C7B	2.6(13)
O2	C3	C3A	C4A	62.8(3)	C5	C6	C7	S1	39.1(4)
O2	C3	C3A	C7A	177.5(2)	C5	C6	C7	C7A	-65.0(4)
N2	C1	C7A	C3A	-0.7(2)	C6	C7	C7A	C1	-54.3(3)
N2	C1	C7A	C7	114.52(19)	C6	C7	C7A	C3A	61.0(3)
N2	C1	C7A	C7B	114.52(19)	C7	S1	C4	C3A	-61.45(15)
N2	C3	C3A	C4	-116.60(19)	C7	S1	C4	C5	49.8(2)
N2	C3	C3A	C4A	-116.60(19)	C5A	C6A	C7B	S1A	-44.6(10)
N2	C3	C3A	C7A	-1.9(2)	C5A	C6A	C7B	C7A	59.9(10)
N2	C8	C9	C10	177.81(18)	C6A	C7B	C7A	C1	-173.2(5)
N2	C8	C13	C12	-178.16(17)	C6A	C7B	C7A	C3A	-57.9(6)
C1	N2	C3	O2	-177.9(2)	C7A	C3A	C4	S1	44.45(18)
C1	N2	C3	C3A	1.5(2)	C7A	C3A	C4	C5	-62.7(3)
C1	N2	C8	C9	108.3(2)	C7A	C3A	C4A	S1A	-48.7(2)
C1	N2	C8	C13	-73.8(2)	C7A	C3A	C4A	C5A	59.9(6)
C3	N2	C1	O1	178.54(19)	C8	N2	C1	O1	-6.0(3)
C3	N2	C1	C7A	-0.5(2)	C8	N2	C1	C7A	175.00(17)
C3	N2	C8	C9	-76.7(2)	C8	N2	C3	O2	6.6(3)
C3	N2	C8	C13	101.3(2)	C8	N2	C3	C3A	-173.99(17)
C3	C3A	C4	S1	158.79(15)	C8	C9	C10	C11	0.4(3)
C3	C3A	C4	C5	51.6(3)	C9	C8	C13	C12	-0.2(3)
C3	C3A	C4A	S1A	65.7(2)	C9	C10	C11	C12	-0.4(3)
C3	C3A	C4A	C5A	174.2(6)	C10	C11	C12	C13	0.1(3)
C3	C3A	C7A	C1	1.6(2)	C11	C12	C13	C8	0.2(3)
C3	C3A	C7A	C7	-119.85(18)	C13	C8	C9	C10	-0.1(3)
C3	C3A	C7A	C7B	-119.85(18)					

Table S13. Bond Lengths for *exo-1(B)*

Atom	Atom	Length/Å	Atom	Atom	Length/Å
S1	C4	1.836(3)	C4	C5	1.519(4)
S1	C7	1.834(3)	C5	C6	1.327(4)
O1	C1	1.209(3)	C6	C7	1.526(4)
O2	C3	1.213(3)	C7A	C7	1.566(4)
N2	C1	1.396(3)	C8	C9	1.387(4)
N2	C3	1.398(3)	C8	C13	1.392(4)
N2	C8	1.434(3)	C9	C10	1.391(4)
C1	C7A	1.511(4)	C10	C11	1.385(4)
C3	C3A	1.519(4)	C11	C12	1.395(4)
C3A	C4	1.563(4)	C12	C13	1.388(4)
C3A	C7A	1.545(4)			

Table S14. Bond Angles for *exo-1(B)*

Atom	Atom	Atom	Angle/°	Atom	Atom	Atom	Angle/°
C7	S1	C4	80.33(13)	C6	C5	C4	110.4(2)
C1	N2	C3	112.8(2)	C5	C6	C7	109.6(2)
C1	N2	C8	122.7(2)	C1	C7A	C3A	105.0(2)
C3	N2	C8	124.1(2)	C1	C7A	C7	111.2(2)
O1	C1	N2	123.9(2)	C3A	C7A	C7	105.5(2)
O1	C1	C7A	127.3(2)	C6	C7	S1	102.22(18)
N2	C1	C7A	108.8(2)	C6	C7	C7A	104.7(2)
O2	C3	N2	124.1(2)	C7A	C7	S1	101.89(17)
O2	C3	C3A	127.4(2)	C9	C8	N2	119.3(2)
N2	C3	C3A	108.5(2)	C9	C8	C13	121.0(2)
C3	C3A	C4	111.2(2)	C13	C8	N2	119.6(2)
C3	C3A	C7A	104.9(2)	C8	C9	C10	119.3(3)
C7A	C3A	C4	105.0(2)	C11	C10	C9	120.2(3)
C3A	C4	S1	101.76(17)	C10	C11	C12	120.2(3)
C5	C4	S1	102.17(18)	C13	C12	C11	120.0(3)
C5	C4	C3A	105.2(2)	C12	C13	C8	119.3(3)

Table S15. Hydrogen Bonds for *exo-1(B)*

D	H	A	d(D-H)/Å	d(H-A)/Å	d(D-A)/Å	D-H-A/°
C3A	H3AA	O2 <sup>1</sup>	1.00	2.57	3.522(3)	159.4
C6	H6A	O1 <sup>2</sup>	0.95	2.45	3.344(3)	155.9
C7A	H7AA	O1 <sup>3</sup>	1.00	2.41	3.338(3)	154.3

<sup>1</sup>1/3+Y-X,2/3-X,-1/3+Z; <sup>2</sup>2/3+Y-X,4/3-X,-2/3+Z; <sup>3</sup>4/3-Y,2/3+X-Y,-1/3+Z

Table S16. Torsion Angles for *exo-1(B)*

A	B	C	D	Angle/°	A	B	C	D	Angle/°
S1	C4	C5	C6	38.4(3)	C3A	C4	C5	C6	-67.5(3)
O1	C1	C7A	C3A	-179.7(3)	C3A	C7A	C7	S1	41.5(2)
O1	C1	C7A	C7	-66.1(3)	C3A	C7A	C7	C6	-64.7(2)
O2	C3	C3A	C4	65.2(3)	C4	S1	C7	C6	50.32(18)
O2	C3	C3A	C7A	178.2(3)	C4	S1	C7	C7A	-57.75(17)
N2	C1	C7A	C3A	-0.8(3)	C4	C3A	C7A	C1	118.5(2)
N2	C1	C7A	C7	112.8(2)	C4	C3A	C7A	C7	1.0(3)
N2	C3	C3A	C4	-114.2(2)	C4	C5	C6	C7	0.3(3)
N2	C3	C3A	C7A	-1.2(3)	C5	C6	C7	S1	-38.9(3)
N2	C8	C9	C10	-178.1(2)	C5	C6	C7	C7A	67.0(3)
N2	C8	C13	C12	178.3(2)	C7A	C3A	C4	S1	-43.0(2)
C1	N2	C3	O2	-178.7(2)	C7A	C3A	C4	C5	63.2(2)
C1	N2	C3	C3A	0.7(3)	C7	S1	C4	C3A	58.49(17)
C1	N2	C8	C9	111.6(3)	C7	S1	C4	C5	-50.11(18)
C1	N2	C8	C13	-66.0(3)	C8	N2	C1	O1	6.2(4)
C1	C7A	C7	S1	-71.8(2)	C8	N2	C1	C7A	-172.7(2)
C1	C7A	C7	C6	-178.0(2)	C8	N2	C3	O2	-6.0(4)
C3	N2	C1	O1	179.0(2)	C8	N2	C3	C3A	173.4(2)
C3	N2	C1	C7A	0.1(3)	C8	C9	C10	C11	0.0(4)
C3	N2	C8	C9	-60.4(3)	C9	C8	C13	C12	0.7(4)
C3	N2	C8	C13	122.0(3)	C9	C10	C11	C12	0.2(4)
C3	C3A	C4	S1	69.9(2)	C10	C11	C12	C13	0.0(4)
C3	C3A	C4	C5	176.1(2)	C11	C12	C13	C8	-0.5(4)
C3	C3A	C7A	C1	1.2(3)	C13	C8	C9	C10	-0.5(4)

**Table S16. Torsion Angles for *exo*-1(B)**

<b>A</b>	<b>B</b>	<b>C</b>	<b>D</b>	<b>Angle/°</b>		<b>A</b>	<b>B</b>	<b>C</b>	<b>D</b>	<b>Angle/°</b>
C3	C3A	C7A	C7	-116.3(2)						

## 5. Computational Chemistry Details

Density functional theory (DFT) calculations have been performed using the *Gaussian 09* package.<sup>1</sup> All theoretical calculations were done by X-ray Cartesian coordinates as initial guess. Wave function calculations for the QTAIM analyses were carried out using the X-ray geometry considering the M062X functionals with DZP-DKH basis set and the Douglas-Kroll-Hess second-order scalar relativistic method (DKH).<sup>2</sup> Using all-electron basis set (DZP-DKH) with relativistic Hamiltonian is the most expensive but most accurate solution for representing electron structure of atoms. The QTAIM calculations were carried out using the Multiwfn 3.8 software.<sup>3</sup> The molecular electrostatic potential (MEP) was calculated with M062X functionals and DZP-DKH basis set. The intrinsic bond strength indicator (ISBI) was also calculated using Multiwfn 3.8 software. The data were visualized using the VMD program.<sup>4</sup> To pursue the nature of the interactions based on the donor-acceptor orbitals, natural bond orbital (NBO) calculations were carried out with PBE1PBE functional and 6-31G\* basis sets for C, H, N, and O atoms and 6-311+G\* basis sets for S atom.<sup>5</sup> The interaction energies were computed for selected dimers retrieved from X-ray structures without optimization based on their noncovalent interactions in the solid state, which has also been successfully used to evaluate the interactions previously.<sup>6</sup> The total interaction energy of the title complex and its associated dimers generated from crystallographic coordinates were elucidated by the energy decomposition analysis (EDA) along with the natural orbitals for chemical valence (ETS-NOCV) using the BP86 functional with Grimme's D3 dispersion correction (D3).<sup>7</sup> To pursue the nature of the interactions based on the donor-acceptor orbitals, natural bond orbital (NBO) calculations were carried out.<sup>8</sup> The triple-zeta quality TZ2P Slater-type basis sets were employed in the conjunction with the zeroth order regular approximation (ZORA) Hamiltonian, as implemented in 2009 version of the ADF software package.<sup>9</sup> For pursuing the nature of the intermolecular interactions, the interactions of ligands were studied by NCIPLOT 3.0 software. It considers the Cartesian coordinates of the interacting molecules by the related intermolecular interactions in their crystal structure and modeling of the pro-molecule density to plot reduced density gradient versus the related electron density multiplied by second Hessian matrix coefficient ( $\text{sign } \lambda_2 \times \rho$ ). The NCI is a visualizing index based on the density and its derivative. It enables identification of non-covalent interactions based on the peaks that appear in the reduced density gradient (s, RDG) at low densities by 2D plotting of its RDG and the related electron density,  $\rho$ .<sup>10</sup>

### 5.1. Intra- and intermolecular interactions

In order to confirm the existence of the intra- and intermolecular interactions, understand the nature of the structure-directing noncovalent interactions in the crystal structure of the synthesized compounds, and quantitatively elucidate its energy from the theoretical approaches, we carried out DFT calculations. The analysis of the anisotropic charge distribution visualized by the molecular electrostatic potential surface

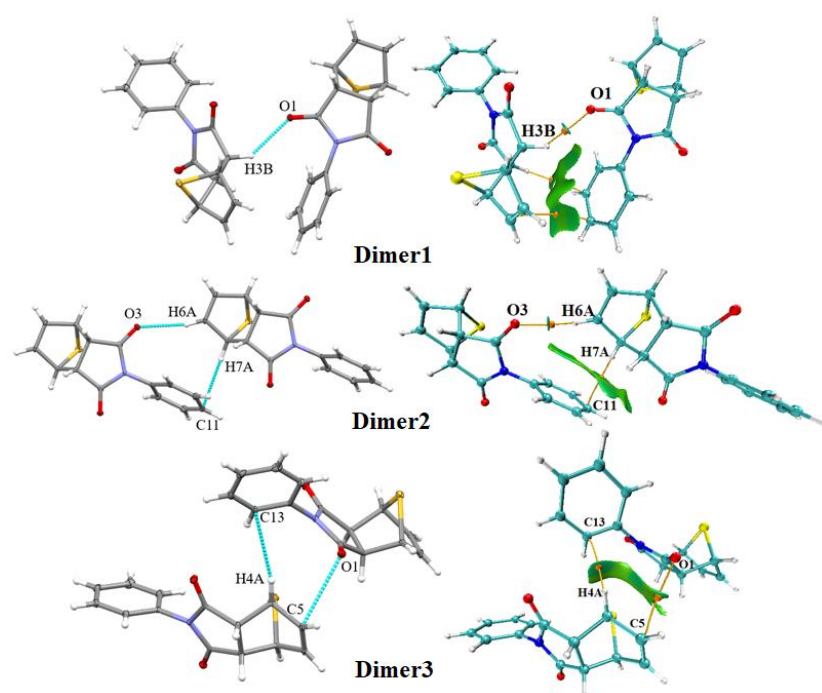
(MEP) which shows the most electron-rich ( $V_{s,\min}$ , red color) and electron-poor ( $V_{s,\max}$ , blue color) regions with negative and positive values of  $V(r)$ , respectively. It can estimate the geometry and strength of the noncovalent interactions. It was also proceed along with the topological analysis of the electron density distribution using Bader's quantum theory of atoms in molecules (QTAIM) for the experimental X-ray geometry of the dimer associates, generated from the Cartesian coordinates of the X-ray structures consolidated by the intermolecular non-covalent interactions. The noncovalent interaction index (NCI) plot analysis of the reduced density gradient (RDG) also was used to show the nature of the intermolecular interactions. The QTAIM analysis of the experimental X-ray geometries of dimeric associates demonstrates the presence of the appropriate bond critical point (3, -1) for the noncovalent interactions. The low magnitude of the electron density (0.0011–0.0099 au), positive values of the Laplacian (0.0072–0.0402 au), and close to zero positive energy density (from 0.0004 to 0.0024 au) at bond critical points (BCP; 3, -1) for the intermolecular interactions proves the noncovalent nature of such interactions which is discussed in details. The defined energies of the contacts proposed by Espinosa *et al.*<sup>11</sup> and Vener *et al.*,<sup>12</sup> confirm the pure noncovalent nature of these interactions. Considering the balance between the Lagrangian kinetic energy  $G(r)$  and potential energy density  $V(r)$  [ $-G(r)/V(r) > 1$ ] at the BCPs and, it suggests that all studied contacts are purely noncovalent. We also used the intrinsic bond strength indicator (IBSI) to confirm the noncovalent interaction nature of the involved atoms as shown in Table S13.<sup>13</sup>

**Table S13.** Values of the density of all electrons  $\rho(r)$ , Laplacian of electron density  $\nabla^2\rho(r)$ , energy density  $H_b$ , potential energy density  $V(r)$ , and Lagrangian kinetic energy  $G(r)$  (Hartree) at the bond critical points (3, -1) for the noncovalent interactions in the structures *exo-1(A)*, **3** and **4**

Contact	$\rho(r)$	$\nabla^2\rho(r)$	$V(r)$	$G(r)$	$H_b$	$E_{\text{int}}$ (Espinosa) <sup>a</sup>	$E_{\text{int}}$ (Vener) <sup>b</sup>	IBSI <sup>c</sup>
<b><i>exo-1(A)</i></b>								
O1...H3B	0.0099	0.0402	-0.0067	0.0084	0.0017	2.10	2.26	0.0134
O3...H6A	0.0079	0.0302	-0.0051	0.0063	0.0012	1.60	1.70	0.0113
O1...C5	0.0052	0.0202	-0.0028	0.0039	0.0011	0.88	1.05	0.0047
<b>3</b>								
O1...H15A	0.0064	0.0239	-0.0039	0.0050	0.0010	1.22	1.35	0.0083
O1...H7	0.0077	0.0333	-0.0052	0.0068	0.0016	1.63	1.83	0.1050
O2...H3A	0.0096	0.0374	-0.0064	0.0078	0.0015	2.01	2.10	0.0126
<b>4</b>								
O1...H7B	0.0011	0.0396	-0.0071	0.0085	0.0014	2.23	2.89	0.0137
O2...N2	0.0085	0.0399	-0.0053	0.0076	0.0024	1.66	2.04	0.0063
O2...C3	0.0025	0.0072	-0.0010	0.0014	0.0004	0.31	0.38	0.0093
H3A...C13	0.0079	0.0263	-0.0044	0.0055	0.0011	1.38	1.48	0.0079
H3A...C8	0.0028	0.0101	-0.0010	0.0018	0.0007	0.31	0.48	0.0084

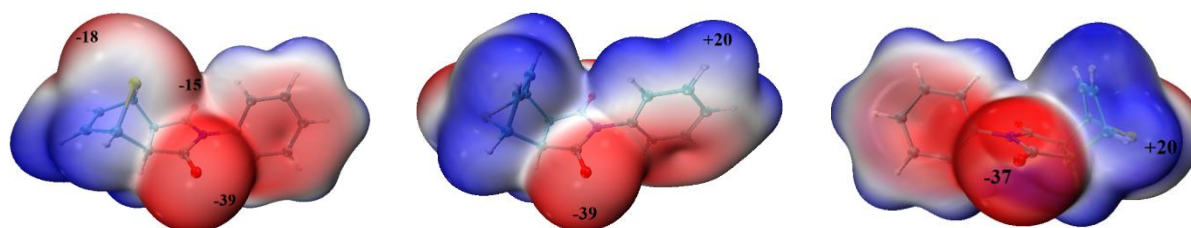
<sup>a</sup>  $E_{\text{int}} = -V(r) / 2$ ; <sup>b</sup>  $E_{\text{int}} = 0.429 G(r)$ ; <sup>c</sup> Intrinsic Bond Strength Index

The QTAIM analysis of the experimental X-ray geometries of dimeric associates demonstrates the presence of the appropriate bond critical point (3, -1) for the noncovalent interactions. In the *exo-1(A)* polymorph, there are three dimer associates connected by non-classic C–H···O hydrogen bonds. The low electron density and Laplacian values of these interactions confirm their noncovalent nature. The low interaction energy based on Esponisa and Vener schemes in the dimer associates confirms non-classic nature of such hydrogen bonding. The low ISBI values (0.0083–0.1050) of such interactions also noncovalent interactions. The X-ray generated dimers and their theoretical structures are shown in Fig. S4.



**Figure S4.** X-ray generated dimers (right) and visualization of the overlay of AIM and NCI plot analysis for the dimer associates of the *exo-1(A)* structure (right), showing C–H···O and C–H··· $\pi$  interactions with the related RDG surfaces with pale-bluish green in the BCPs with  $0.25 \text{ (e}^{1/3} \text{ Bohr)}^{-1}$  values were colored from blue [ $\text{sign}(\lambda_2)\rho = -0.03 \text{ e/Bohr}^3$ ] to red [ $\text{sign}(\lambda_2)\rho = 0.03 \text{ e/Bohr}^3$ ]

The MEP distributions around the surface of *exo-1(A)*, **3** and **4** polymorphs are shown in Fig. S5.



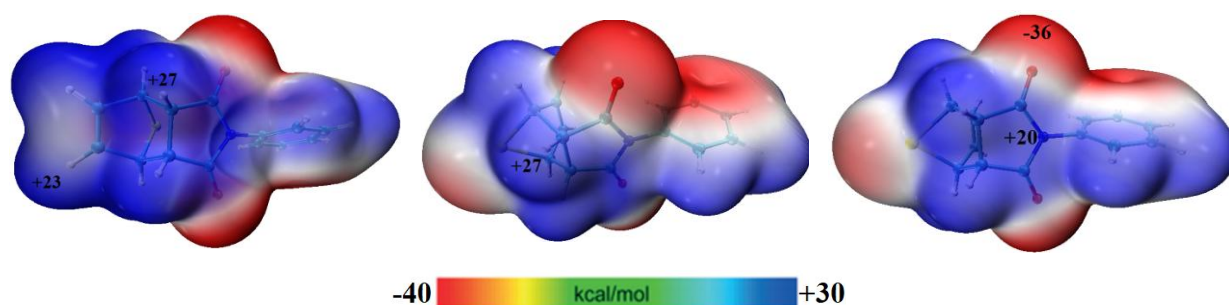


**Figure S5.** Molecular electrostatic potential (MEP) calculated at the M062X/DZP-DHK computational level on the 0.001 au molecular surface of the top (the top row) and down (the bottom row) view of the compounds *exo-1(A)* (on the left), **3** (in the center) and **4** (on the right)

In the mixed crystals **3**, there are also three dimer associates connected by non-classic C–H···O hydrogen bonds. The low electron density and Laplacian values of these interactions confirm their noncovalent nature. The low interaction energy based on Espinosa and Vener schemes in the dimer associates confirms non-classic nature of such hydrogen bonding. The low ISBI values (0.0064–0.0096) of such interactions also confirm their noncovalent interactions. The X-ray generated dimers and their theoretical structures are shown in Fig. S6.

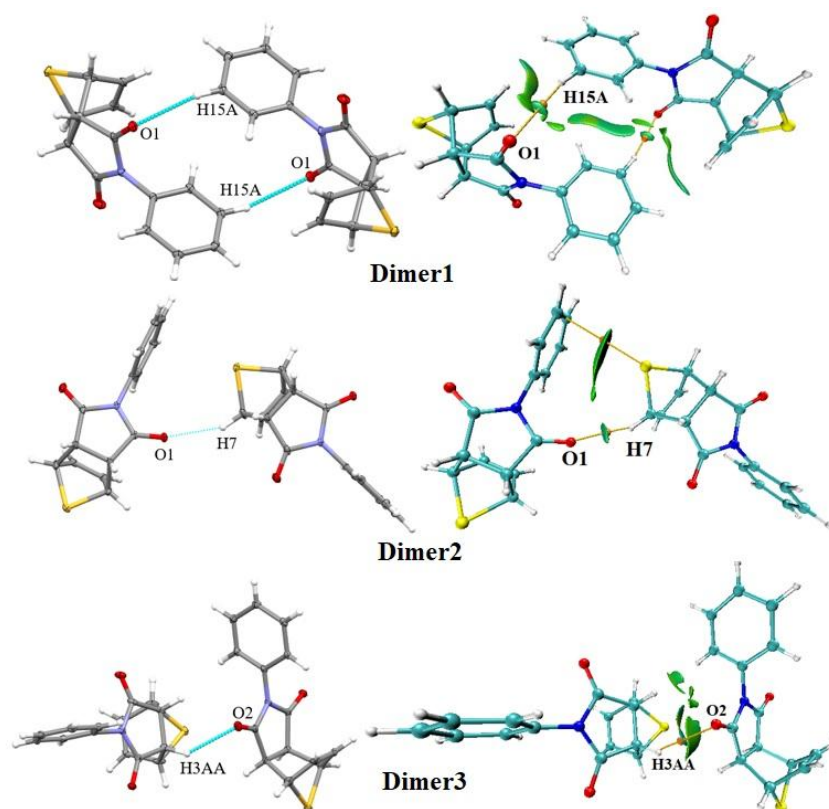


**Figure S6.** Visualization of the overlay of AIM and NCI plot analysis for the dimer associates of the mixed crystals **3** in X-ray (left) and theoretical (right) structures, showing C–H···O and C–H··· $\pi$  interactions with the related RDG surfaces with pale-bluish green in the BCPs with  $0.25 \text{ (e}^{1/3} \text{ Bohr)}^{-1}$  values were colored from blue [ $\text{sign}(\lambda_2)\rho = -0.03 \text{ e/Bohr}^3$ ] to red [ $\text{sign}(\lambda_2)\rho = 0.03 \text{ e/Bohr}^3$ ]

In the mixed crystals **4**, there are also three dimer associates connected by non-classic C–H $\cdots$ O hydrogen bonds and C–H $\cdots$  $\pi$  contacts. The low electron density and Laplacian values of these interactions along with the low value of the ISBI also confirm their noncovalent nature. The low interaction energy based on Esponisa and Vener schemes in the dimer associates confirms non-classic nature of such hydrogen bonding. The X-ray generated dimers and their theoretical structures are shown in Fig. S7. For the Dimer 2 of the mixed crystals **3**, we also used natural bond orbital calculations to pursue the nature and energy of the proposed  $n \rightarrow \pi^*$  interaction between the lone pair of O2 and the C3=O2 carbonyl group.

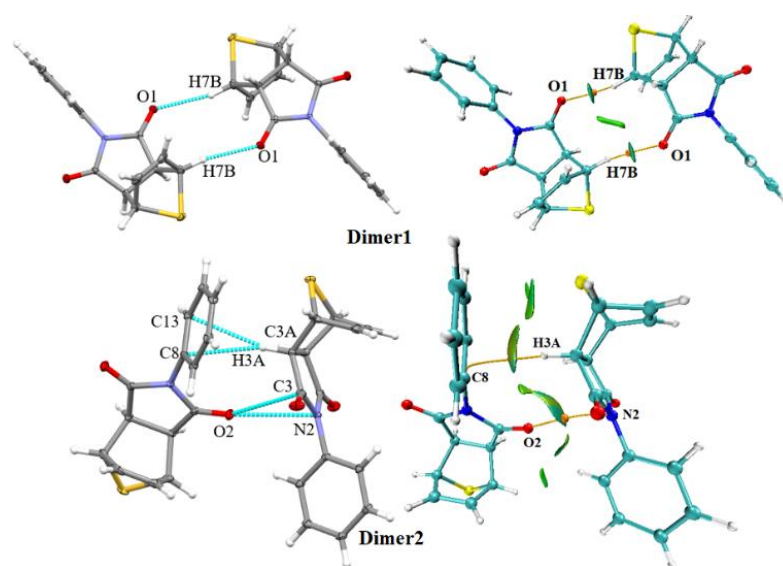


**Figure S7.** Visualization of the overlay of AIM and NCI plot analysis for the dimer associates of the mixed crystals **4** in X-ray (left) and theoretical (right) structures, showing C–H $\cdots$ O,  $n \rightarrow \pi^*$ , and C–H $\cdots$  $\pi$  interactions with the related RDG surfaces with pale-bluish green in the BCPs with  $0.25 \text{ (e}^{1/3} \text{ Bohr)}^{-1}$  values were colored from blue [ $\text{sign}(\lambda_2)\rho = -0.03 \text{ e/Bohr}^3$ ] to red [ $\text{sign}(\lambda_2)\rho = 0.03 \text{ e/Bohr}^3$ ]

The overlap of the lone pair of the oxygen atom with contribution from  $s$  and  $p$ -orbitals and the  $\pi^*$ -orbital of the carbonyl group [ $n_s(\text{O}2) \cdots \pi^*(\text{C}3=\text{O}2)$  and  $n_p(\text{O}2) \cdots \pi^*(\text{C}3=\text{O}2)$ ] of the adjacent molecules are depicted in Fig. S8. These interactions account for a total energy release of  $0.85$  and  $0.41 \text{ kcal}\cdot\text{mol}^{-1}$  according to the NBO analysis from second-order perturbation energy, respectively.

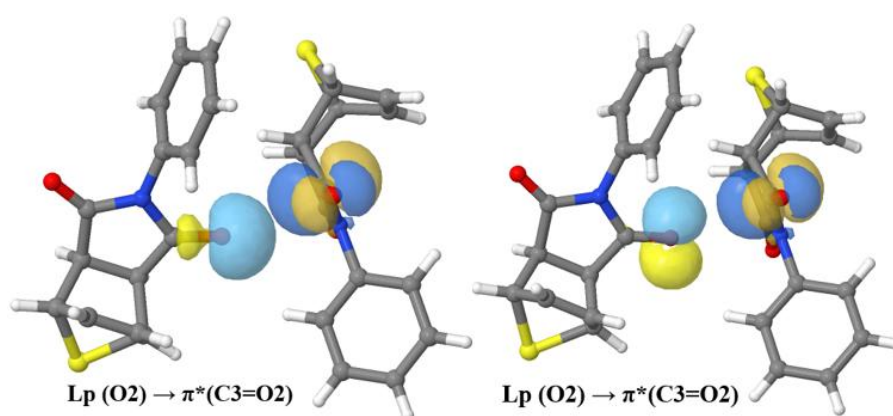


**Figure S8.** Intermolecular  $n \rightarrow \pi^*$  interactions (donor-acceptor orbitals) between the lone pair of the oxygen ( $n_s$  and  $n_p$ ) and  $\pi^*$  orbital of the carbonyl group.

## 5.2. Interaction energy and energy decomposition analysis (EDA)

Following the structural analysis of the intermolecular interactions in the dimer associates resulted from crystallographic coordinates, we have selected the dimer associates of the three polymorphs connected by the non-covalent interactions to pursue the total noncovalent interaction energy ( $\Delta E_{\text{int}}$ ) between the monomers which are mainly consolidated by the intermolecular  $C-H \cdots O$ ,  $C-H \cdots \pi$ , and  $n \rightarrow \pi^*$  contacts. The dimer associates generated from the X-ray structure were shown in Figs. S4, S6, S7 in the left columns. Furthermore, the interaction energy is decomposed (EDA) into Pauli repulsion ( $\Delta E_{\text{Pauli}}$ ), electrostatic ( $\Delta E_{\text{elstat}}$ ), orbital interactions ( $\Delta E_{\text{orb}}$ ) and dispersion energy ( $\Delta E_{\text{disp}}$ ) terms. This method was originally developed by Morokuma<sup>14</sup> and further modified by Ziegler and Rauk,<sup>15</sup> calculations were performed in conjunction with the NOCV (natural orbital for chemical valence) method using the ADF program package.

**Table S14.** Energy decomposition analysis parameters in ( $\text{kcal} \cdot \text{mol}^{-1}$ ). Values in parenthesis correspond to the percentage of each stabilizing contribution ( $\Delta E_{\text{elstat}} + \Delta E_{\text{orb}} + \Delta E_{\text{disp}} = 100\%$ ) for the dimer associates in *exo-1(A)*, **3**, and **4**, respectively.

Entry	$\Delta E_{\text{int}}$	$\Delta E_{\text{Pauli}}$	$\Delta E_{\text{elstat}}$	$\Delta E_{\text{orb}}$	$\Delta E_{\text{disp}}$
<b>exo-1(A)</b>					
Dimer 1	-6.77	6.38	-3.40 (26%)	-2.09 (16%)	-7.66 (58%)
Dimer 2	-8.28	6.44	-4.91 (33%)	-2.40 (17%)	-7.42 (50%)
Dimer 3	-11.22	9.29	-6.27 (31%)	-3.17 (15%)	-11.06 (54%)
<b>3</b>					
Dimer 1	-8.75	7.64	-3.93 (24%)	-2.67 (16%)	-9.79 (60%)
Dimer 2	-4.84	4.04	-2.70 (17%)	-1.45 (9%)	-4.74 (29%)
Dimer 3	-9.17	7.15	-5.09 (31%)	-2.66 (16%)	-8.58 (53%)
<b>4</b>					
Dimer 1	-6.37	5.78	-5.51 (45%)	-2.46 (20%)	-4.18 (35%)
Dimer 2	-12.17	12.11	-7.64 (32%)	-3.91 (16%)	-12.73 (52%)

The results of the energy decomposition analysis ( $\text{kcal} \cdot \text{mol}^{-1}$ ) for the dimer associates are summarized in Table S14. The results show that the total bonding energy in all dimer associates are attractive, with the overall negative binding energy. In the dimer associates, except in one case

for the Dimer 1 of mixed crystals **4** with 35% contribution, which is less than electrostatic contribution of 45%, the London dispersion part is in fact the major contributor of the overall stabilization energy, overcoming  $\Delta E_{\text{Pauli}}$  and making the interaction attractive. Electrostatic-based charge-delocalization contribution further contributes to the stability of the dimer aggregates. The conclusion is that the  $\Delta E_{\text{disp}}$  term is the most important attractive energy component of the overall binding energy in these dimer aggregates.

## 6. X-ray phase analysis of polycrystalline samples *exo-1B*, *endo-1* and mixed crystals **3**

To verify the phase homogeneity of the synthesized compounds and mixed crystals, powder X-ray diffraction (PXRD) patterns were acquired.

X-ray phase analysis of polycrystalline samples *exo-1(B)*, *endo-1* and mixed crystals **3** was performed using a Dandong Tongda TD-3700 X-ray diffractometer (CuK $\alpha$  radiation, Ni filter, linear detector) at room temperature over a  $2\theta$  range of  $7^\circ$  to  $30^\circ$  (Figs. S9–S11).

The experimental diffraction pattern of the polycrystalline sample *exo-1(B)* (Fig. S9, at the top) was compared with the calculated diffraction pattern (at the bottom), which was derived from the single-crystal X-ray structure of *exo-1(B)* obtained at 100 K (CCDC # 2424425). The superimposed patterns are presented in Fig. S9, demonstrating good agreement between the experimental and simulated data.

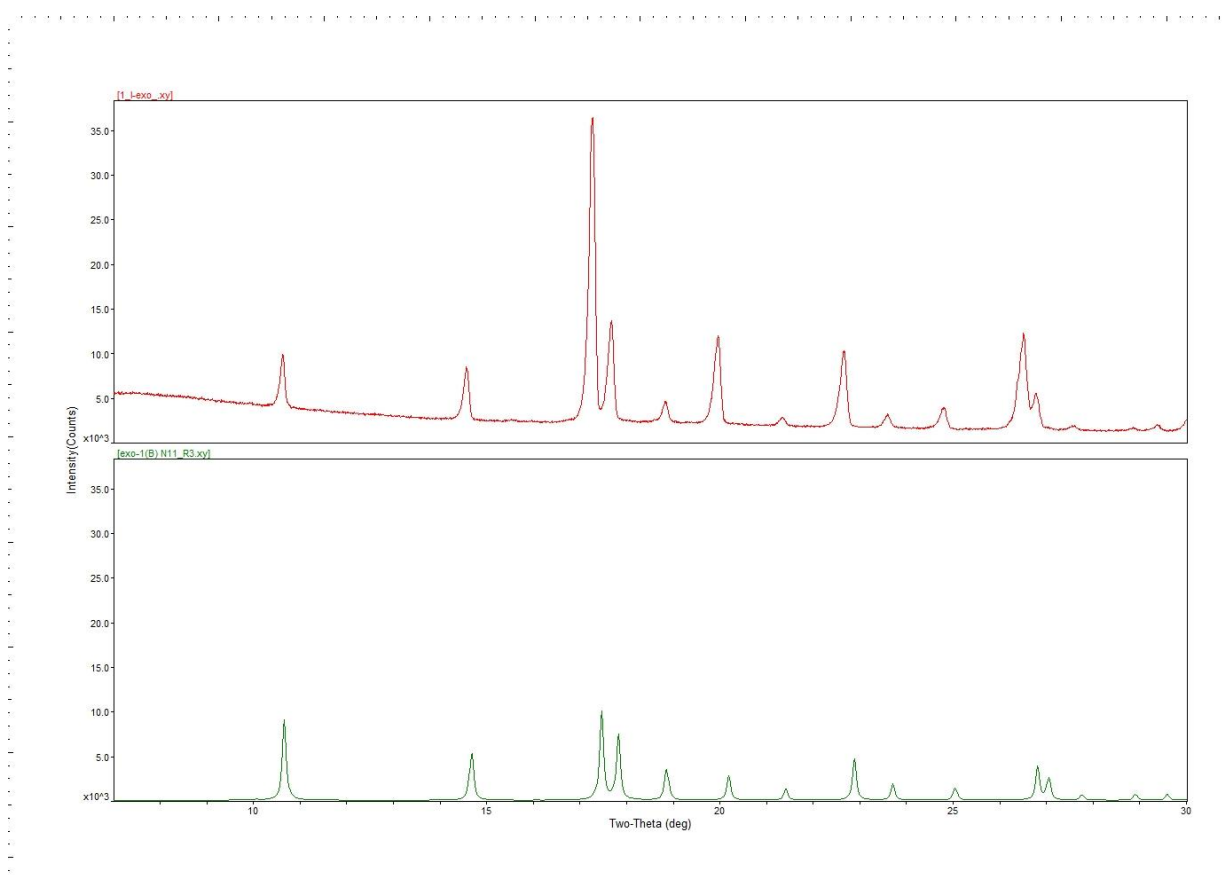


**Figure S9.** Diffraction patterns of polycrystalline *exo-1(B)*: (top red line) experimental pattern obtained at room temperature and simulated pattern derived from single-crystal X-ray diffraction data (bottom green line)

The diffraction patterns of *exo-1(B)* (Fig. S10) demonstrate excellent agreement between the experimental (polycrystalline, room temperature) and simulated (single-crystal, T = 100 K) data, confirming the phase purity of the compound. A minor peak shift is observed, attributable to subtle variations in unit cell parameters between the polycrystalline and single-crystal samples, likely caused by the temperature difference (300 K vs. 100 K).

The experimental diffraction pattern of the polycrystalline sample *endo-1* (Fig. S10, in the top) was compared with the calculated diffraction pattern (in the bottom), which was derived from the single-crystal X-ray structure of *endo-1* obtained at 100 K (CCDC # 607356). The superimposed patterns are presented in Fig. S10, demonstrating good agreement between the experimental and simulated data.

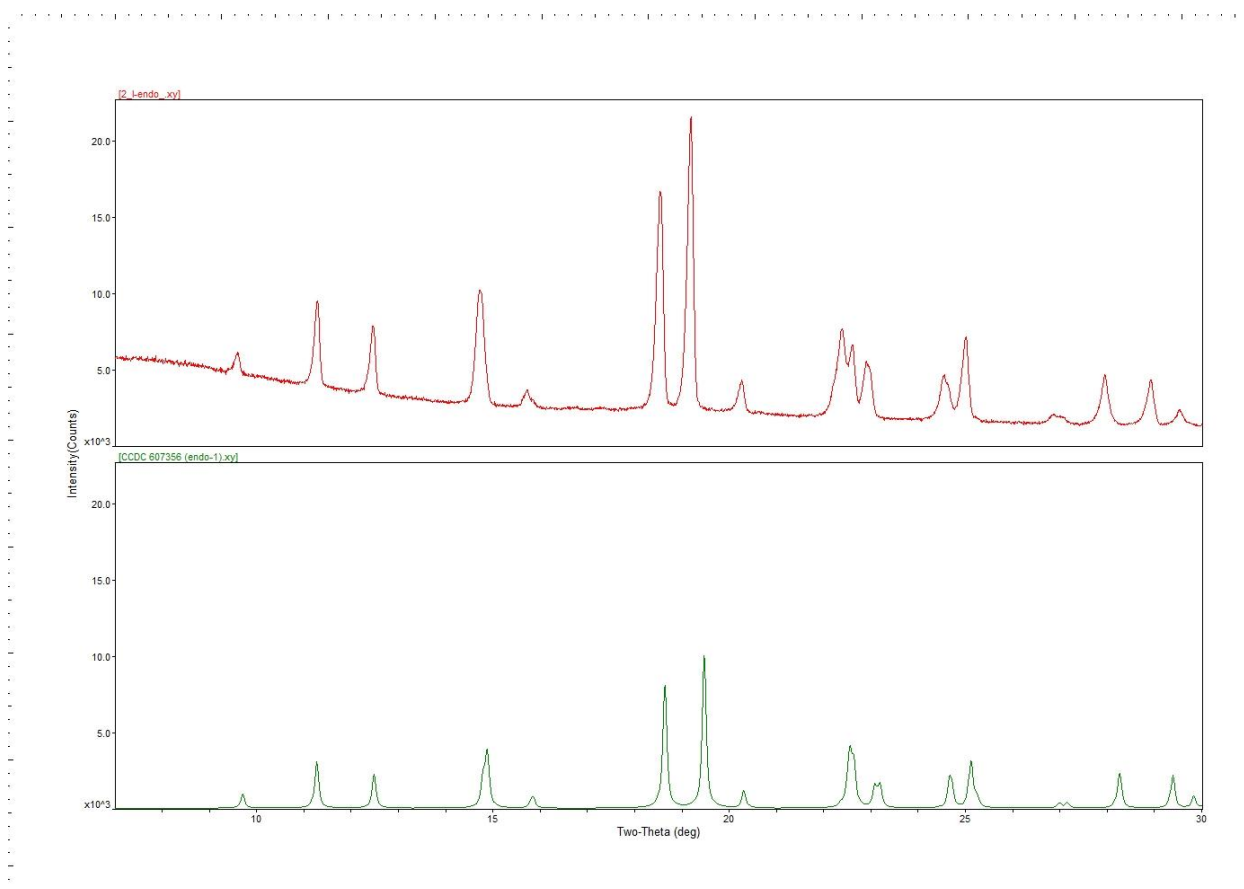


**Figure S10.** Diffraction patterns of polycrystalline *endo-1*: (top red line) experimental pattern obtained at room temperature and simulated pattern derived from single-crystal X-ray diffraction data (bottom green line)

The experimental powder diffraction pattern of mixed crystals **3** (Fig. S11, at the bottom) shows only partial agreement with the simulated pattern (in the top), derived from the single-crystal X-ray structure of **3** obtained at 100 K (CCDC # 2391533). This discrepancy arises from two factors: (1) the limited quantity of sample available for analysis (was collected by Pasteur's method), and (2) the incomplete separation of phase **3** from other polymorphic forms.

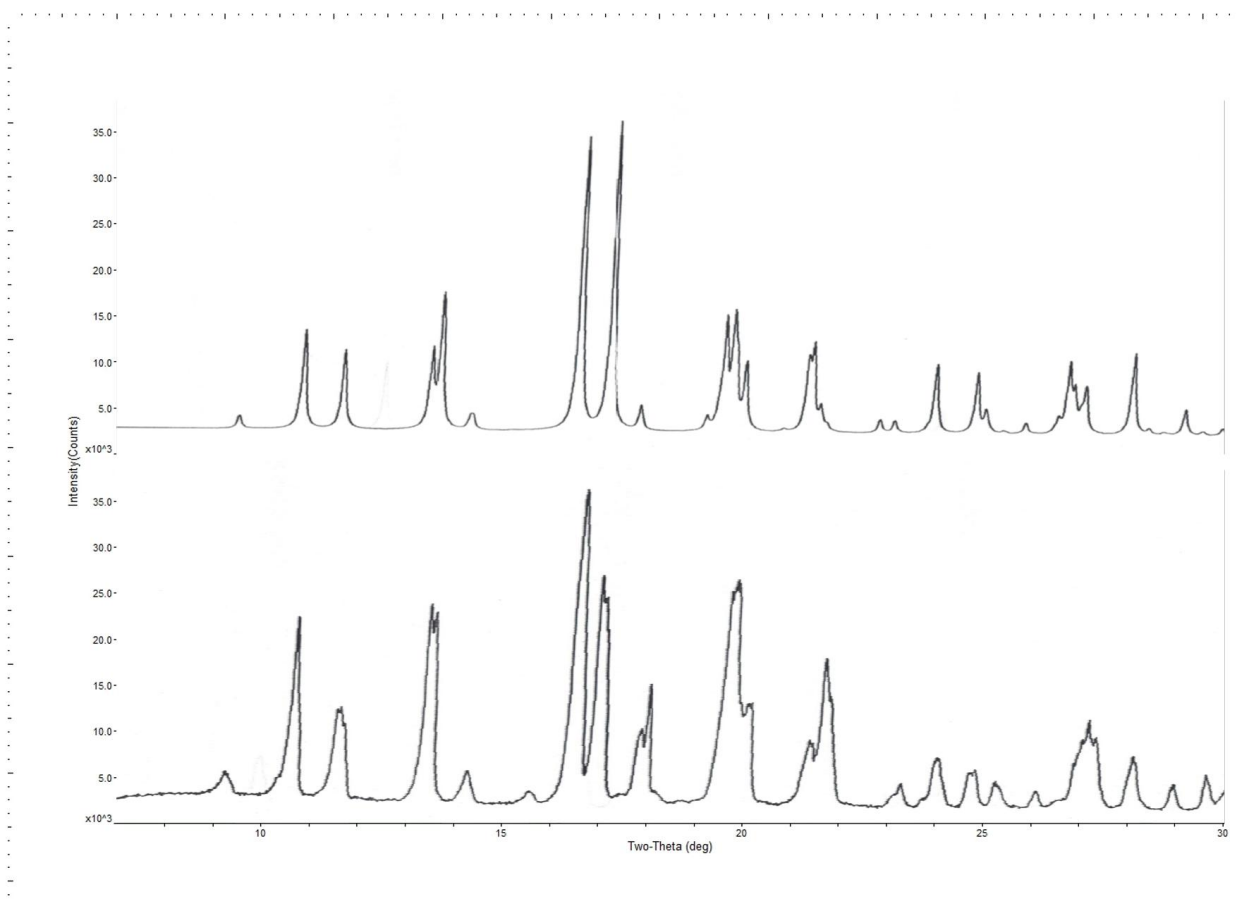


**Figure S11.** Diffraction patterns of polycrystalline **3**: experimental pattern obtained at room temperature (at the bottom) and simulated pattern derived from single-crystal X-ray diffraction data (at the top)

## References for ESI

1. M. J. Frisch, G. W. Trucks, H. B. Schlegel, G. E. Scuseria, M. A. Robb, J. R. Cheeseman, G. Scalmani, V. Barone, B. Mennucci, G. A. Petersson, H. Nakatsuji, M. Caricato, X. Li, H. P. Hratchian, A. F. Izmaylov, J. Bloino, G. Zheng, J. L. Sonnenberg, M. Hada, M. Ehara, K. Toyota, R. Fukuda, J. Hasegawa, M. Ishida, T. Nakajima, Y. Honda, O. Kitao, H. Nakai, T. Vreven, J. A. Montgomery, Jr., J. E. Peralta, F. Ogliaro, M. Bearpark, J. J. Heyd, E. Brothers, K. N. Kudin, V. N. Staroverov, T. Keith, R. Kobayashi, J. Normand, K. Raghavachari, A. Rendell, J. C. Burant, S. S. Iyengar, J. Tomasi, M. Cossi, N. Rega, J. M. Millam, M. Klene, J. E. Knox, J. B. Cross, V. Bakken, C. Adamo, J. Jaramillo, R. Gomperts, R. E. Stratmann, O. Yazyev, A. J. Austin, R. Cammi, C. Pomelli, J. W. Ochterski, R. L. Martin, K. Morokuma, V. G. Zakrzewski, G. A. Voth, P. Salvador, J. J. Dannenberg, S. Dapprich, A. D. Daniels, O. Farkas, J. B. Foresman, J. V. Ortiz, J. Cioslowski and D. J. Fox, 2009, *Gaussian*, Inc., Wallingford CT.

2. F. E. Jorge, A. Canal Neto, G. G. Camiletti and S. F. Machado, *J. Chem. Phys.* 2009, **103**, 064108.
3. T. Lu and F. W. Chen, *J. Comput. Chem.* 2012, **33**, 580–592.
4. W. Humphrey, A. Dalke and K. Achulten, *Mol. Graphics* 1996, **14**, 33–38.
5. B. P. Pritchard, D. Altarawy, B. Didier, T. D. Gibson and T. L. Windus. *J. Chem. Inf. Model.* 2019, **59**, 4814–4820.
6. P. Chakraborty, S. Purkait, S. Mondal, A. Bauzá, A. Frontera, C. Massera and D. Das, *CrystEngComm* 2015, **17**, 4680–4690.
7. S. Grimme, A. Hansen, J. Gerit Brandenburg, and Ch. Bannwarth, *Chem. Rev.* 2016, **116**, 5105–5154.
8. (a) E. D. Glendenning, C. R. Landis and F. Weinhold, *WIREs Comput. Mol. Sci.* 2012, **2**, 1–42; (b) S. Tsuzuki and T. Uchimaru, *Phys. Chem. Chem. Phys.* 2020, **22**, 22508–22519.
9. G. Frenking and F. M. Bickelhaupt, *The EDA perspective of chemical bonding. In The Chemical Bond: Fundamental Aspects of Chemical Bonding.* 2014, **1**, 121–158.
10. (a) E. R. Johnson, S. Keinan, P. Mori-Sánchez, J. Contreras-García, A. J. Cohen and W. Yang, *J. Am. Chem. Soc.* 2020, **132**, 6498–6506; (b) J. Contreras-García, E. Johnson, S. Keinan, R. Chaudret, J. Piquemal, D. Beratan and W. Yang, *J. Chem. Theory Comput.* 2011, **7**, 625–632.
11. E. Espinosa, E. Molins and C. Lecomte, *Chem. Phys. Lett.* 1998, **285**, 170–173.
12. M. V. Vener, A. N. Egorova, A. V. Churakov and V. G. Tsirelson, *J. Comput. Chem.* 2012, **33**, 2303–2309.
13. J. KleinHassan, K.-Ch. Boisson, J. Contreras-García, J-P. Piquemal, and E. Hénon, *J. Phys. Chem. A* 2020, **124**, 1850–1860.
14. K. Morokuma, *J. Chem. Phys.* 1971, **55**, 1236–1244.
15. T. Ziegler and A. Rauk, *Inorg. Chem.* 1979, **18**, 1755–1759.